INTERPLAY OF FINITE SIZE AND STRAIN ON THERMAL CONDUCTION

INTERPLAY OF FINITE SIZE AND STRAIN ON THERMAL CONDUCTION

By TAHEREH MAJDI, M.A.Sc.

A thesis submitted to the school of Graduate Studies in Partial Fulfilment of the Requirements for the Degree of Doctor of Philosophy

McMaster University

McMaster University DOCTOR OF PHILOSOPHY (2019) Hamilton, Ontario (Engineering Physics)

TITLE: Interplay of finite size and strain on thermal conduction

AUTHOR: Tahereh Majdi, B. Eng. (McMaster University), M.A.Sc. (McMaster University)

SUPERVISOR: Dr. Ishwar Puri

NUMBER OF PAGES: xxiii - 83

Lay abstract

Since strain changes the interatomic spacing of matter and alters electron and phonon dispersion, an applied strain ϵ can modify the thermal conductivity κ of a material. This thesis shows how the strain induced by heteroepitaxy is a passive mechanism to change κ in a thin film and how the film thickness is key to the functional form of $\kappa(\epsilon)$. Molecular Dynamics simulations of the physical vapor deposition and epitaxial growth of ZnTe thin films provide insights into the role of interfacial strain on the thermal conductivity of a deposited film. The result is relevant to thermoelectric devices since strain can also enhance charge mobility and increase their overall efficiency. The resulting understanding of $d\kappa/dT$ shows that strain engineering can also be used to create a thermal rectifier in a material that is partly strained and partly relaxed, like at the junction of an axial nanowire heterostructure.

Abstract

Since strain changes the interatomic spacing of matter and alters electron and phonon dispersion, an applied strain ϵ can modify the thermal conductivity κ of a material. This thesis shows how the strain induced by heteroepitaxy is a passive mechanism to change κ in a thin film and how the film thickness is key to the functional form of $\kappa(\epsilon)$. Molecular Dynamics simulations of the physical vapor deposition and epitaxial growth of ZnTe thin films provide insights into the role of interfacial strain on the thermal conductivity of a deposited film. ZnTe films grown on a lattice mismatched CdTe substrate exhibit ~6% in-plane biaxial tension and ~7% out-of-plane uniaxial compression. In the T=700 K to 1100 K temperature range, the conductivities of strained ZnTe layers that are 5 unit cells thick decrease by ~ 35%, a result that is relevant to thermoelectric devices since strain can also enhance charge mobility and increase their overall efficiency. The resulting understanding of $d\kappa/dT$ shows that strain engineering can also be used to create a thermal rectifier in a material that is partly strained and partly relaxed, like at the junction of an axial nanowire heterostructure.

To better isolate the role of strain, the study is extended to free-standing ZnTe films with thicknesses between 116 Å to 1149 Å under the application of both uniform and biaxial strain between -3% to 3% at 300 K. Since the boundaries of the film are diffuse, κ becomes size dependent when the film thickness approaches the order of the mean free path of the phonons. As this thickness is decreased, the magnitude of κ decreases until boundary scattering dominates so that $\kappa(\epsilon)$ depends on $v_g(\epsilon)$. This conclusion is important as it can be generalized to other materials and potential functions; it suggests that if a film is

thin enough for boundary scattering to dominate, then the behavior of $\kappa(\epsilon)$ can be predicted based on the bulk dispersion curve alone, which should greatly simplify strain-based device design.

Acknowledgements

I am forever grateful that Professor Puri invited me into his group and mentored me, as my PhD was an amazing journey, one that stimulated growth and aspirations. Along the way, I began a fruitful and cherished collaboration with Professor Preston and his team and received guidance from Professor Mascher, which were instrumental to how my thesis formed. I shared my journey with an outstanding team of family, friends, colleagues, faculty, and staff, all who supported me along the way and contributed to my successes.

I have been told that I am somewhat unconventional. In keeping with tradition, my gratitude follows.

Thank you for being my family, cheering me on along every step, motivating me, and reminding me of all the great things in life.	*Thank you for being a team player. Lending an extra hand when I needed it or being an optimist when skies were grey.*	*Thank you for inspiring and mentoring me when I needed it most. It went a long way.*	*Thank you for teaching me something new, facilitating my research, and helping me maneuver technical challenges.*	*Thank you for being amazing administers and facilitating everyday tasks.*
Haftshijani, Mansour	Abdalla, Ahmed	Jovanovic, Stephen	Andrei, Carmen	Laidler, Robert
Haftshijani, Mila	Abdel Fattah, Abdel Rahman	Korjani, Mohammad	Brewick, Clealand	Macdonald, Nicole
Jovanovic, Andrew	Aithal, Srivasta	Majdi, Abbas	Britten, James	Maltese, Diana
Jovanovic, John	Chen, Ri	Majdi, Mahin	Butcher, Chris	Marlow, Marilyn
Jovanovic, Kathy	Fattahi, Arash	Mascher, Peter	Cahill, David	Novosedlik, Sarah

Jovanovic, Paul	Ghosh, Suvojit	McConvey, Margo	Chan, Mattew	
Jovanovic, Stephen	Gupta, Tamaghna	Preston, John	Chin, Kenrick	
Majdi, Abbas	Jangid, Krishana	Puri, Ishwar	Cino, Mike	
Majdi, Edris	Meleca, Elvira		Dames, Chris	
Majdi, Fatima	Mishriki, Sarah		Drake, David	
Majdi, Mahin	Navar, Mohammad		Dube, Paul	
Majdi, Maryam	Nayak, Suchitra		Duft, Andy	
Melanson, Melissa	Pal, Souvik		Ebos, Seth	
	Pang, Huingfang		Garret, Jim	
	Sahu, Rakesh		Ghukasyan, Ara	
	Tsai, Jennifer Peiying		Hafreager, Anders	
	Puri, Ishwar		Hahn, Mark Hahn	
			Hodges, Wyatt	
			Hu, Ming	
			Jarvis, Victoria	
			Jonasson, Peter	
			Jovanovic, Stephen	
			Kleiman, Rafael	
			Korinek, Andreas	
			Kuyanov, Paul	
			LaPierre, Ray	
			Luke, Graeme	
			Mascher, Peter	
			Minnick, Matt	
			Murad, Sohail	
			Nedialkov, Ned	
			Oliveira, Pedro	
			Pal, Souvik	
			Preston, John	

			Puri, Ishwar	
			Sahu, Rakesh	
			Stevanovic, Doris	
			Tavakoli, Shahram	
			Xiaowang, Zhou	
			Yuen, Avery	

This thesis is dedicated to my amazing mom and dad, Mahin and Abbas Majdi, my brother Edris, my sister Fatima, my niece Mila, and my soulmate Stephen Jovanovic.

Contents

List of figures

List of tables

List of abbreviations and symbols

a	Chapter 1: acoustic mode Chapter 2, 3, and 4: lattice constant Chapter 5: slope of a linear approximation to thermal conductivity vs. temperature
aaa	acoustic-acoustic scattering creating an acoustic wave
aao	acoustic-acoustic scattering creating an optical wave
$a - o$	acoustic-optic band gap
B	bulk modulus
b	y-intercept of a linear approximation to thermal conductivity vs. temperature
C	heat capacity per unit volume
c_{ph}	phonon specific heat
D	thickness of the finite dimension
e_{eff}	effective charge
$\mathbf{F}$	force
f	relative length fraction of one material to the total length
h	Planck's constant
J	heat flux
$\mathbf{k}$	phonon modes
k_B	Boltzmann constant
l	scattering length
l_b	boundary scattering
L	length
LA	longitudinal acoustic
LO	transverse optic
m	mass
$\bar{M}$	average atomic mass
MD	Molecular Dynamics
n	number of atoms per primitive cell
$o1 - o2$	band gap between the longitudinal and acoustic optic modes

p	polarization
P	pressure
$\mathbf{q}$	phonon mode
$\mathbf{r}$	displacement
r	atomic radius
R	thermal rectification
S	Seebeck coefficient
SW	Stillinger-Weber
T	temperature
TA	transverse acoustic
TO	transverse optic
V	volume
v_g	group velocity
y	relative position within a material
ZT	thermoelectric figure of merit
α	thermal expansion coefficient
γ	Grüneisen parameter
$\tilde{\gamma}_\infty$	high temperature Grüneisen parameter averaged over the acoustic branch
Δt	timestep
δ	average atomic volume
ϵ	strain
θ	Chapter 4: angle between atomic bonds Chapter 5: non-dimensional temperature
θ_D	Debye temperature
$\tilde{\theta}_\infty$	Debye temperature for acoustic modes at high temperature
κ	thermal conductivity
κ_0	unstrained thermal conductivity
ν	frequency
σ	electrical conductivity
τ	relaxation time
Φ	interatomic potential function

Declaration of academic achievement

Most of Chapter 2 and section 3.2.2 of this thesis is based on the manuscript *Altering thermal transport by strained-layer epitaxy* by T. Majdi, S. Pal, A. Hafreager, S. Murad, R.P. Sahu, I.K. Puri, published in Applied Physics Letters, May 2018 [1]. T. Majdi developed the hypothesis, wrote the LAMMPS (Large-scale Atomic/Molecular Massively Parallel Simulator) Molecular Dynamics (MD) simulation scripts, wrote custom Python scripts to analyze and perform error analysis on the MD data, developed the discussion, and wrote the manuscript. A. Hafreager introduced a more efficient method for simulating thermal conduction measurements of free-standing thin films. He assisted in writing the scripts pertaining to *Figure 12* and engaged in several useful discussions toward this work. Dr. S. Pal, assisted with learning LAMMPS and provided mentorship along with Professor I.K. Puri, Professor S. Murad, and Dr. R. Sahu throughout the project. They all assisted with editing the manuscript and provided useful feedback.

The theory, appendix A, and appendix B sections of Chapter 5 are based on the manuscript *Recipe for optimizing a solid-state thermal rectifier* by T. Majdi, S. Pal, I.K. Puri published in the International Journal of Thermal Sciences, July 2017. S. Pal suggested the framework, S. Pal and T. Majdi developed the analytical equation, and T. Majdi implemented it to configure Figure 22. I.K. Puri and S. Pal provided mentorship throughout this project. T. Majdi wrote the manuscript and all the authors edited it and provided useful feedback.

The remaining sections, unless referenced, were hypothesized, analyzed, and written by T. Majdi. Professor Preston engaged in several useful discussions pertaining to Chapters 3 and 4 and Professor Puri provided mentorship for all chapters.

Chapter 1 Background

1. Heat transport in matter

Thermal energy is transferred by conduction, convection, and/or radiation. Conduction refers to heat transfer within a medium while convection is heat transfer between a surface and a moving fluid that is at a different temperature. All surfaces of nonzero temperature emit electromagnetic waves so there is a net heat transfer by radiation between surfaces at different temperatures.

The following sections build up the theoretical background for heat transfer by conduction which is the focus of this thesis.

1.1. Thermal conduction

Thermal conduction is the transfer of energy from more energetic to less energetic particles due to interactions between particles. In steady state, the thermal energy flux J is proportional to the product of thermal conductivity κ and the temperature gradient ∇T, i.e. $J = -\kappa \nabla T$. The diffuse nature of energy propagation caused by frequent scattering events is evident from the proportionality of J to ∇T instead of ΔT. If heat transfer was not diffuse, then the length would not matter. For an isotropic material, combining this equation with the Boltzmann transport equation under certain approximations gives

$$\kappa = \frac{1}{3} \sum_p \sum_{\mathbf{k}} c_{ph} v_g(\mathbf{k}, p) l(\mathbf{k}, p), \qquad \text{(Eq.1)}$$

where the summations are over all phonon modes $\mathbf{k}$ and all polarizations p and v_g is the group velocity, l is the mean free path, and c_{ph} is the phonon specific heat for each mode [2], [3]. A material is more thermally conductive when phonons can store more energy (c_{ph}) and transfer that energy at a higher velocity (v_g), before scattering (l). In a simplified theory based on kinetic theory of gases, the dependence of thermal conductivity on polarization and normal mode of vibration is neglected and the thermal conduction along the x, y, or z direction for a cubic system simplifies to

$$\kappa = \frac{1}{3} C v_g l, \tag{Eq.2}$$

where C is the heat capacity per unit volume.

1.2. Scattering of thermal waves

1.2.1 Thermal waves in matter

Thermally driven vibrations in one atom propagate through a medium by virtue of the interatomic forces. Considering the atomistic nature of a medium, allows one to study the allowed vibrational modes, density of states of the vibrational modes, and their dispersion, i.e. the energy of a wave as a function of its direction of propagation. Detailed descriptions are found in references [4] and [5].

There are two types of thermal waves, acoustic and optic as shown in Figure 1. They are further categorized based on their polarization. Waves created by atoms vibrating perpendicular to the direction of propagation are called transverse waves, while if they vibrate parallel to the direction of propagation, the waves are longitudinal. Each acoustic and optical wave will have two transverse (TA1 or a_{T1}, TA2 or a_{T2}, TO1 or o_{T1}, and TO2 or o_{T2}) and one longitudinal mode (LA and LO).

Acoustic waves are generated by atoms and their center of mass moving together similar to long acoustical vibrations. [4] Optical waves are created by atoms vibrating against each other, but their center of mass is fixed. Optical phonons are exclusive to crystals with two or more atoms per primitive cell. The two atoms at nonequivalent lattice sites do not have to differ in mass but should differ in either mass or force constant. If the atoms are of opposite charge, this motion can be excited by an electric field of light, hence the name optical waves. [4] If the lattice crudely represents an ionic crystal with two atoms types that are ions of opposite charge then their vibrations will create large electric moments which generate electromagnetic waves in the infrared spectrum

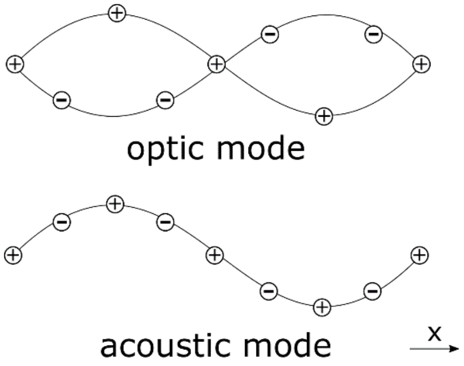

Figure 1. Schematic of transverse acoustic and transverse optical waves propagating along the x-direction. The optical mode is generated by atoms vibrating against each other while the acoustic mode is generated by atoms moving in the same direction. The figure is modified from [4].

In a cubic system, the two TA branches do not differ greatly in velocity due to the symmetry of the crystal, while the LA branch will have the largest velocity. This is because longitudinal waves are compression waves for which the elastic restoring forces are stronger than the transverse shear waves. [2] An example is shown in the figure below. The same notions typically apply to optical modes.

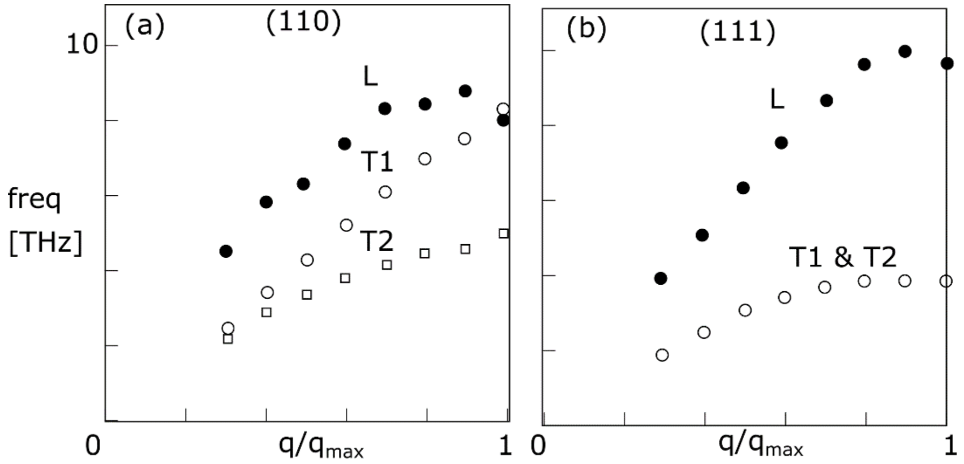

Figure 2. Dispersion curves for different acoustic polarization branches of aluminum. (a) Wave propagation is along the [110] direction. Atoms are vibrating parallel to the [001] direction for T_1 and the are propagating along the $[1\bar{1}0]$ direction for T_2. Since Al is an FCC crystal the atomic configuration is not symmetric along these two directions and the two transverse modes are distinguishable. (b) The wave propagation is along the [111] direction. The transverse waves overlap because of the symmetry along the $[1\bar{1}0]$ and the $[\bar{1}10]$ direction. The figure is modified from [6].

1.2.2. Intrinsic scattering

Intrinsic thermal resistance in nonmetals arises from the anharmonicity of the interatomic potential, which leads to non-conservative phonon scattering known as Umklapp scattering. The presence of a lattice wave causes a periodic elastic strain which through anharmonic interactions modulates the elastic constant of the crystal in both space and time. A secondary lattice wave encounters the modulated elastic constant and is scattered, producing a third wave. [4]

Based on conservation of energy, there are no scattering processes in which all three phonons belong to the same polarization branch of the spectrum; the created phonon must lie in a higher branch than at least one of the destroyed phonons. *aaa* scattering is possible if $a_{\mathrm{T}} + a_{\mathrm{T}} \rightarrow a_{\mathrm{L}}$ and $a_{\mathrm{T}} + a_{\mathrm{L}} \rightarrow a_{\mathrm{L}}$ [2].

Conservation of energy also limits scattering with optical modes. Optical modes commonly have larger frequencies than the acoustic mode. This prevents $a + o \rightleftarrows a$ and $o + o \rightleftarrows a$. The group velocity of acoustic modes is larger than optical modes, so $a + o \rightleftarrows o$ is forbidden by an extension of the rule that the created phonon must lie in a higher branch than at least one of the annihilated phonons. The only remaining processes involving optical modes are of $a + a \rightleftarrows o$ which are possible if the optical frequencies are not so high that no combination of acoustic frequencies would have their energy. Let A_{max} and O_{max} denote the maximum acoustic and optical frequencies respectively. Using a simple Debye-Einstein model it can be shown that Umklapp scattering involving optical modes increases as O_{max}/A_{max} increases until O_{max} becomes so large that no two acoustic modes can combine to reach O_{max}. As O_{max}/A_{max} approaches 2, the number of Umklapp processes decrease to zero. In practice, this effect is seen by varying the mass ratio of the atoms in an ionic crystal. [2]

A larger mass ratio is attributed to a larger gap between the optic and acoustic modes of phonon dispersion. This can be shown easily for a linear diatomic chain [4] and has been experimentally measured for zincblende systems; see Figure 3 (a) Furthermore, the energy of the longitudinal optical branch is increased relative to the transverse optical branch by increasing ionicity [7]; see Figure 3 (b).

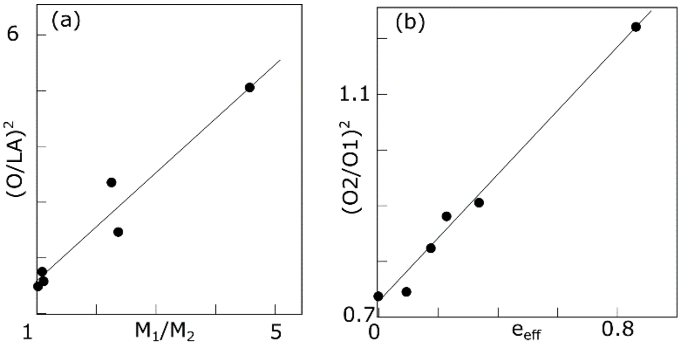

Figure 3. (a) The effect of mass difference on the *a-o* gap in the thermal wave dispersion curve. (b) Effect of ionicity on the *o2-o1* gap. Where the numbers 1 and 2 distinguish the acoustic and longitudinal optical branches and $\mathrm{e_{eff}}$ denotes the effective ionic charge. Images modified from [7].

1.2.3. Boundary scattering

Finite dimensions in thermal transport equations are imposed as boundary conditions that reflect the incident carriers. In practice, the diffusivity at the boundary depends on the detailed structure of the surface and the mode of propagation, but typically, a simple phenomenological description is used; a fraction s of the incident carriers are specularly reflected while the remainder are scattered. The reflectivity can be set to 1 for specular reflection or 0 for perfectly diffuse and uniform scattering in all directions without reference to the direction of the incident wave. The relaxation time τ_B for boundary scattering is given by

$$\frac{1}{\tau_B} = \frac{v_g}{D}(1 - s), \tag{Eq. 3}$$

where D is the characteristic dimension. If the effect of confinement on v_g can be neglected, the scattering length caused by the boundaries becomes

$$l_b = \frac{D}{1-s}, \tag{Eq. 4}$$

so boundary scattering off a perfectly specular interface will not reduce thermal conduction.[8] When the surface is perfectly rough, we arrive at the Casimir limit, where the surface absorbs all incident phonons and re-emits them at a rate depending on the absolute temperature according to the theory of black-body radiation. In general, if we wish to calculate transport properties of a solid undergoing different scattering processes, the total resistivity is approximated as the sum of resistivities due to each type of scattering. If a single mean free path l is defined for each type of scatter, then the total mean free path is given by

$$\frac{1}{l} = \frac{1}{l_1} + \frac{1}{l_2} + \cdots, \tag{Eq. 5}$$

known as Matthiessen's rule. Let l_∞ denote the mean free path for internal scattering averaged over all the wave vectors, and l_b denote the mean free path for boundary scattering, then the total mean free path is estimated by [2]

$$\frac{1}{l} = \frac{1}{l_\infty} + \frac{1}{l_b}. \tag{Eq.6}$$

1.3. Molecular dynamics simulations of heat transport

Molecular Dynamics (MD) simulations numerically solve the differential equations of motion

$$\frac{m_i d^2\mathbf{r}_i}{dt^2} = \mathbf{F}_i = -\frac{\partial \Phi}{\partial \mathbf{r}_\mathrm{i}} \qquad \text{(Eq.7)}$$

for a system of atoms, where m, $\mathbf{r}$, $\mathbf{F}$ are mass, displacement, and force of the i^{th} atom, and Φ is the interatomic potential. Thus, MD is a classical deterministic method to model the behavior of a system. The inputs are atomic positions, velocities, and the interatomic potential function. By solving the equations of motion in timesteps Δt the displacement and velocities are dynamically evaluated and are used to determine temperature, kinetic energy, potential energy, vibrational spectrum, etc. The time step should be small enough to capture the effect of the highest frequency vibrations (f_{max}); a time step smaller than $\frac{1}{10 f_{\mathrm{max}}}$ is sufficient. The atomic vibrations follow Boltzmann statistics, which is the high-temperature limit of Bose-Einstein statistics. Furthermore, MD simulations capture the full anharmonicity of atomic interactions, making this technique relevant above the Debye temperature. [9] Thermal conductivity can be calculated in various ways however in this thesis a non-equilibrium method is used whereby some of the atoms in the system are used as a heat source and sink by setting their average temperature or heat flux. The slope of the temperature profile between the heat source and sink, the heat flux, and cross-section area are used to evaluate thermal conduction. The simulations should run sufficiently long until further increase in averaging time does not appreciably change the results. Details on the method for calculating thermal conductivity and the vibrational spectrum are provided Chapters 2 and 3.

1.2. Thermal Conductivity vs. Strain

1.2.1. Common trends

In 1924 Bridgman published the first known measurements of thermal conductivity versus hydrostatic pressure for several non-metallic compounds and showed that thermal conductivity increased with pressure [10]. Since then, several materials such as KCl, KBr, [11] CsCl, NaCl,[12], Si [13], and MgO [14] have been measured and thermal conductivity was found to increase with pressure. Theoretical calculations[15] and molecular dynamics simulations [16],[17] supported this trend, suggesting that this was a universal feature.[18]

The observed trend is justified by a simple equation for thermal conductivity provided by Leibfried, Schlömann, and Julian. The theory assumes that heat is carried by acoustic phonons and only aaa scattering occurs. This model is reasonable for rare-gas crystals as they only have one atom per primitive cell, i.e. optical modes do not exist. It is questionable for diamond-like and rock-salt structures with two atoms per primitive cell as the second atom in the primitive cell gives rise to optical phonons. Regardless, it has been applied to several semiconducting compounds and falls within ±40% of experimental values. For two or more atoms per primitive cell the equation is

$$\kappa(T) = Bn^{\frac{1}{3}}\,\bar{M}\delta\tilde{\theta}_{\infty}^{3}/(T\tilde{\gamma}_{\infty}^{2}) \qquad \text{(Eq.8)}$$

where B is a constant, n is the number of atoms per primitive cell, $\bar{M}$ is the average atomic mass, $\delta^3 = a_0^3/4n$ is the average volume occupied by one atom of the crystal, $\tilde{\theta}_{\infty}$ is the Debye temperature for the acoustic branch at high temperatures, and $\tilde{\gamma}_{\infty}$ is the high temperature Grüneisen parameter averaged over the acoustic branch only. [19] Under compression, the vibrational frequencies increase and so does $\tilde{\theta}_{\infty}$, and the material stiffens so $\tilde{\gamma}_{\infty}$ reduces. The increase in $\tilde{\theta}_{\infty}^{3}/\tilde{\gamma}_{\infty}^{2}$ compensates for the reduction in a_0 under compression and increases thermal conduction.[18]

This theory is limited as it does not consider aao phonon scattering, so the conclusions are not universal. As described below thermal conductivity may also increase under compression.

1.2.2. Anomalies

In some materials, thermal conduction reduces under pressure, but the reasons are not well understood. Slack experimentally observed $\frac{d\kappa}{dP} < 0$ in CuCl, [20] and H_2O_{solid} [21] and attributed it to the negative γ_{TA}, although, this is not a sufficient condition since many tetrahedral cubic semiconductors have negative γ_{TA}, [22] but $\frac{d\kappa}{dP}$ may be positive such as in ZnS.[23] Furthermore, the function $\kappa(P)$ depends on T since γ is a function of T. $\gamma < 0$ when the negative effect of γ_{TA} is larger than the positive effect of γ_{LA}. From Eq. 8, $\frac{d\kappa}{dV} = 3\gamma + \frac{2d\gamma}{dV} - \frac{1}{3} \approx 5\gamma - \frac{1}{3}$, [19] so if $\gamma < 0$ then $\frac{d\kappa}{dV} < 0$. The negative γ_{TA} indicates a decrease in stiffness of the lattice of the TA modes under compression and is related to the first-order pressure induced phase transition from zinc blend to white-tin or NaCl type structure.[22]

Lindsay et al. performed first principle calculations of pressure-dependent phonon thermal transport in a large range of III-V and II-VI cubic compounds and attributed the anomaly of $\frac{d\kappa}{dP} < 0$ to the non-existent *aao* scattering processes at all pressures, combined with an increase in aaa scattering processes caused by the separation of the transverse and longitudinal acoustic branches.[18]

Ouyang and Hu combine first principle calculations and Boltzmann transport equation to show that at a given temperature, the pressure response of κ for a material depends on the competition between the enhanced group velocity of the longitudinal acoustic and optic modes and the reduction of the phonon relaxation time of the transverse acoustic modes. When the negative γ of the transverse acoustic modes dominates the enhancements of thermal conductivity of the group velocity, $\frac{d\kappa}{dV} < 0$. [24]

The commonality between the above is that in all cases, $\frac{d\kappa}{dV} < 0$ is associated with an increase in *aaa* scattering. Slack, Ouyang, and Hu directly associate the increase in *aaa* with the negative γ, while Lindsay ascribes it to the increase in phase space which may or may not be caused by a negative γ. Furthermore, Lindsay attributes the enhancement of κ with P to the upward shift of the optical bands, which increases the optical-acoustic (*a-o*) bandgap and reduces *aao* scattering processes in small bandgap materials. The size of the *a*-o gap depends, in-part, on $m_{\text{heavy}}/m_{\text{light}}$ which suggests that at high mass ratios the *a-o* gap becomes large enough that *aao* scattering is non-existent. Under pressure the transverse and longitudinal acoustic branches separate and increase *aaa* processes which reduce thermal conduction. In their study of compounds with a mass ratio of 1.07 to 14.16, they only find the reduction with pressure for mass ratios of larger than ~3. All cases were studied far away from the phase transition pressure [18] It is interesting to note that CuCl which also shows $\frac{d\kappa}{dV} < 0$, is a zincblende structure with a mass ratio of 1.8

which is about half the value found by Lindsay et al. [18] and is also measured away from its phase transition [20].

In essence, a change in volume can either increase or decrease κ by changes in both the v_g and l. The theory for when or why this occurs is not well understood.

1.3 Organization of this thesis

Chapter 2 studies the significance of heteroepitaxial strain on altering thermal conduction. MD simulations of the physical vapor deposition of ZnTe on CdTe and ZnTe are conducted and followed by non-equilibrium MD simulations to determine the thermal conductivity of the relaxed and strained deposited ZnTe crystal. Chapter 3 extends this study by simulating ZnTe at different film thicknesses and under different amounts of strain, both biaxial and uniform, to develop a general understanding of the effect of strain on thermal conduction. In Chapter 4, parameters for validating the potential function for thermomechanical MD simulations is discussed and its importance is highlighted. Chapter 5 looks at a new application of strain for inducing thermal rectification and Chapter 6 summarizes this thesis.

2. Altering thermal conductivity by strained-layer epitaxy

Most of this chapter is reproduced from T. Majdi, et. al, “Altering thermal transport by strained-layer epitaxy,” *Appl. Phys. Lett.*, vol. 112, no. 19, 2018.and its supplemetary material, with the permission of AIP Publishing.

2.1. Introduction

It is possible to alter a material’s thermal conductivity κ through passive and nondestructive mechanisms. Altering κ can be useful to modulate heat dissipation in integrated electronics or for thermoelectrics that require low κ but high electrical conductivity. [25] [26]'[27]'[28] Furthermore, tuning $d\kappa/dT$ is relevant in designing thermal rectifiers, where the heat flux depends on the direction of the temperature gradient.[29]' [30] We utilize the strain induced by heteroepitaxy as a passive method to alter κ in a thin film. Since this mechanism of strain induction can be realized in practice, it has practical relevance for device design. Previous experiments indicate that $SrTiO_3/CaTiO_3$ superlattices grown on $NdGaO_3$ have a larger thermal conductivity than when the superlattices are grown on $SrTiO_3$ substrates. The measured difference in κ is attributed to the different in-plane strains of -0.1% and 0.93% that are produced for the two cases, respectively. [31]'[32] Our systematic simulations unambiguously quantify the effect of heteroepitaxial strain on κ. Unlike existing heat transfer literature for lattice mismatched heterostructures,[33], [34] this entry simulates the complete cycle of thin film deposition and growth, evaluates the deposited film’s thermal conductivity, and in

Chapter 5 the applicability of epitaxy-induced strain for a thermal rectifying device is evaluated.

Molecular Dynamics (MD) simulations are employed to investigate the deposition and growth of thin films [35] and their thermal responses.[16], [36] The atomic coordinates of the substrate are specified *a priori*. As the constituent atoms are deposited, an epitaxial thin film grows with a crystallographic orientation that is influenced by the substrate. During homoepitaxy, both the thin film and substrate are composed of the same crystals so that the film-substrate lattice parameters are perfectly matched. Hence, the material does not experience interfacial-bond straining. In the case of heteroepitaxy, the film and substrate materials are different and thus have mismatched lattice parameters. Depending on the deposition conditions, extent of lattice mismatch and thickness of the deposited film, the interfacial adatoms of the film can either become strained or relaxed by forming dislocation defects at the interface. [37]

Specifically, we consider strained-layer epitaxy in ZnTe-CdTe heterostructures, with both materials being wide bandgap II-VI semiconductors used in optoelectronic devices. [38], [39] Their heterostructures have a lattice mismatch of $(a_{\mathrm{su}} - a_{\mathrm{f}})/a_{\mathrm{f}} \approx 6\%$, where the subscripts su and f denote the substrate and thin film respectively. This mismatch is small enough to allow high quality crystal growth, but sufficiently large to unambiguously reveal changes in κ. Hence, these materials provide an ideal case to explore the influence of strained-layer epitaxy on κ. For reference, we also simulate the homoepitaxial growth of relaxed ZnTe films and compare their thermal responses with those of the strained heteroepitaxial ZnTe films grown on CdTe substrates. Both the homoepitaxial and heteroepitaxial grown films are dislocation free. Nonequilibrium MD studies provide κ for the ZnTe films, which are evaluated between 700-1100 K. These temperatures lie well below the melting points of ZnTe (1568 K) and CdTe (1315 K) [40] and exceed their Debye temperature values θ_D, i.e., ZnTe (225 K) and CdTe (158 K) [41], ensuring that the MD simulations are relevant.

2.2. Methods

2.2.1. Overview

The simulations are conducted using LAMMPS [42] and employ the Zn-Cd-Hg-S-Se-Te Stillinger-Weber potential that appropriately reproduces experimental lattice constants, cohesive energies and elastic constants, while ensuring that the lowest energy structure is tetrahedral.[43]

An overview of the MD simulations is presented in Figure 4. First, as shown in Figure 4(a), simulations are performed with a 0.4 fs time step under constant NPT – number of atoms, pressure, and temperature – with periodic boundaries to determine the equilibrium lattice constant of the substrate between 700-1100 K. The substrate is either ZnTe or CdTe with a zincblende crystal structure. In this temperature range, the equilibrium lattice constant of CdTe ranges from 6.507-6.525 Å and for ZnTe from 6.133-6.155 Å. For reference, lattice constants for both materials are also evaluated at 293 K and found to be only 0.1% larger than experimental measurements at ~300 K but the lattice mismatch between ZnTe and CdTe agrees with experiments. The slight overestimate of the lattice parameters is characteristic of the potential function employed. [44],[35] Table 1 contains a full list of the measured lattice constants.

Subsequent simulations, presented in Figure 4 (b), use these values for the lattice constants. The periodic *x* and *y* boundaries are 5 unit cells wide, the *z* boundary is fixed and 18 unit cells high, and the bottom most layer is fixed and immobile. The substrate is equilibrated to 1200 K for 5-10 ns under constant NVT – number of atoms, volume, and temperature – using Nosé-Hoover style thermostats[45][46]. The substrate thermostatting continues until 3 ns after deposition whereupon 1 Zn and 1 Te atom are introduced from the top of the simulation box every 55 ps with an incident angle of 0° and an incident energy of 5.3 eV – 6 eV. The accelerated deposition rate makes it computationally feasible to simulate the physical vapor deposition of a film, however, it reduces surface diffusion. This is mitigated by elevating the substrate temperature to 1200 K which increases surface diffusion and allows for the growth of high quality crystalline films [47]. Following deposition, the deposited thin film and the substrate are equilibrated for 5-10 ns with a time step of 0.5 fs to the average temperature at which κ is measured. The distribution of atomic species, lattice spacing and potential energy per atom are measured along the *z* axis.

The system is further equilibrated at constant NVE – number of atoms, volume, and energy – for 0.5-1 ns. The last 10^4 steps are spaced at 1.0 fs to record instantaneous atomic velocities which are later processed to determine the vibrational spectrum. Finally, nonequilibrium MD is employed to determine κ_{ZnTe} with a heat source and sink, as shown in in Figure 4 (b), and the non-thermostatted region is integrated using NVE with a time step of 0.5 fs. The thermal conductivity $\kappa = J\left(\frac{dT}{dz}\right)^{-1}$, where J denotes the heat flux and the gradient dT/dz is determined through a linear fit to the temperature profile that is averaged over 40 ns. The standard deviations of the temporal and spatial measurements are used as uncertainty measures for all the disclosed parameters. The time steps used for these simulations are conservative since, based on the vibrational spectrum presented later, a larger time step may be used, although the velocity of the deposited atoms should also be considered when optimizing the time step. Further details of the simulation methodology and the influence of the size of the simulation box are provided in the following sections.

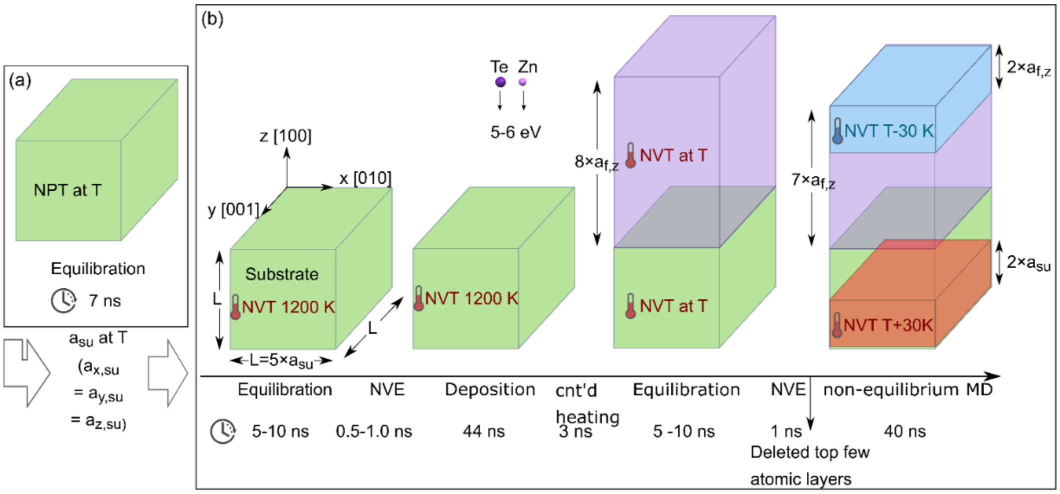

Figure 4: Simulation overview. (a) Simulations are conducted using periodic boundary conditions, under NPT, to determine the equilibrium lattice constant. The substrate is a Zincblende crystal, either Zn-terminated (upper most surface) ZnTe, or Cd-terminated CdTe. The calculated lattice constants are used as inputs into subsequent simulations shown in (b). a_{su} and $a_{\mathrm{f,z}}$ denote the substrate and thin film lattice constants along the z-direction. For homoepitaxy, $a_{\mathrm{f,z}} = a_{\mathrm{su}}$, and for heteroepitaxy, with CdTe as the substrate, $a_{\mathrm{f,z}} < a_{\mathrm{su}}$. The x and y boundaries in (b) are periodic while the z boundary is fixed. Figure reproduced from [1], with the permission of AIP Publishing.

2.2.2. Measuring equilibrium lattice constant

Simulations are performed for bulk ZnTe and CdTe structures in an NPT ensemble, to determine their equilibrium lattice constants at various temperatures. Under constant atmospheric pressure the system can expand or contract to its equilibrium lattice spacing. The length of the simulation box divided by the number of unit cells provides the average lattice constant in the x, y, and z directions. These constants are used as inputs for the simulations concerning deposition and κ. For the NPT simulations, the pressure is constant at 10^5 Pa and once for reference at 0 Pa. The lattice constants are evaluated at temperatures, varying from 273 K to 1200 K. At each temperature, the simulations are performed for 7 ns. Data are averaged and recorded every 100 ps. The first 4 ns of the simulation allow the system to equilibrate, while the final 3 ns are used to average the lattice constants and find their standard deviations. Each simulation constitutes 8 × 8 × 8 [(unit cells)^3], periodic boundaries, and a time step of 0.4 fs. For CdTe, a simulation box of 20 × 20 × 20 [(unit cells)^3] is also evaluated to check for possible size dependence. The measured lattice constants, shown in Table 1, are insensitive to the size of the simulation box.

Table 1: Lattice parameters determined under isothermal and isobaric conditions of 10^5 Pa, unless otherwise specified. The error in all the measurement is ± 0.000 Å which reflects time averaged variations of the lattice constant but does not include systematic errors caused by the potential function. This table modified from the supplementary material in [1], with the permission of AIP Publishing.

	ZnTe 8×8×8 [(unit cells)^3]	**CdTe 8×8×8 [(unit cells)^3]**	**CdTe 20×20×20 [(unit cells)^3]**
300 K from literature	6.103 Å [48]	6.481 Å [49]	6.481 Å [49]
273.15 K	6.111 Å	6.490 Å	6.490 Å
293.15	6.112 Å	6.491 Å	-
600 K	6.118 Å	6.503 Å	-
700 K	6.133 Å	6.507 Å	-
800 K	6.139 Å	6.511 Å	-
900 K	6.144 Å	6.516 Å	-
1000 K	6.150 Å	6.520 Å	6.520 Å
1100 K	6.155 Å	6.525 Å	-
1200 K	6.161 Å	6.529 Å	-
1200 K at 0 Pa	6.161 Å	6.529 Å	-

2.2.3. Measuring equilibrium lattice constant under biaxial strain

Atomic coordinates are recorded every 1 ns in two ways, (1) instantaneously, and (2) averaged for 0.5 ns over coordinates recorded every 0.5 fs. The instantaneous data is used to visualize the atomic structure while the temporally averaged data is further processed to obtain the atomic spacing along the *z*-direction, the surface density, and elemental mixing. Note that only data recorded in the last nanosecond of the second equilibration step are used to evaluate these material properties.

Along the *z*-axis, each atomic layer nominally consists of 50 atoms that are binned together and analyzed as follows. (1) Atomic spacing along the z-direction: the *z*-coordinate of atoms within each bin are averaged. The distance between two subsequent averaged *z*-coordinates provides the atomic layer spacing. (2) Surface density*:* since the surface area is known, the number of atoms per bin divided by the surface area is the surface density. The ideal value for a Zincblende structure is 2 [atoms/unit cells^2]. (3) Atom type distribution*:* the number of Cd, Zn, and Te atoms in each bin is computed and divided by the total number of expected atoms in each bin which is 50 atoms in our simulations.

Along the x- and y-axis, the atomic spacing is computed in two ways. (1) The number of atoms in each atomic layer parallel to the x-z plane is estimated, then used to bin the atoms. The x-coordinate of the atoms in each bin is averaged. The distance between two subsequent x-coordinates provides the atomic layer spacing. The same is repeated for atomic layers that are parallel to the y-z plane. (2) The length of the simulation box divided by the number of unit cells provides the average atomic layer spacing in the x and y directions. Note that this method works when the strain is uniform along the x and y direction.

2.2.4. Deposition

A total of 800 Zn and 800 Te atoms are deposited by introducing 1 Zn and 1 Te atom every 1.1×10^5 time steps of 0.5 fs at random locations through the +*z* boundary of the simulation box. The rapid deposition rate is compensated for by a high substrate temperature of 1200 K during deposition, [47] which allows adatoms to diffuse and grow into high quality crystalline thin films. When an energetic atom impinges on the high temperature substrate or the newly deposited material, momentum transfer may cause sublimation. A reflector is incorporated on the +z-boundary such that the sublimated material is reflected toward the substrate, so it is eventually reincorporated into the film. This prevents loss of atoms during the simulation and reduces the total deposition time. Figure 5 presents two dimensional projections of the homoepitaxial growth of ZnTe at various times during deposition.

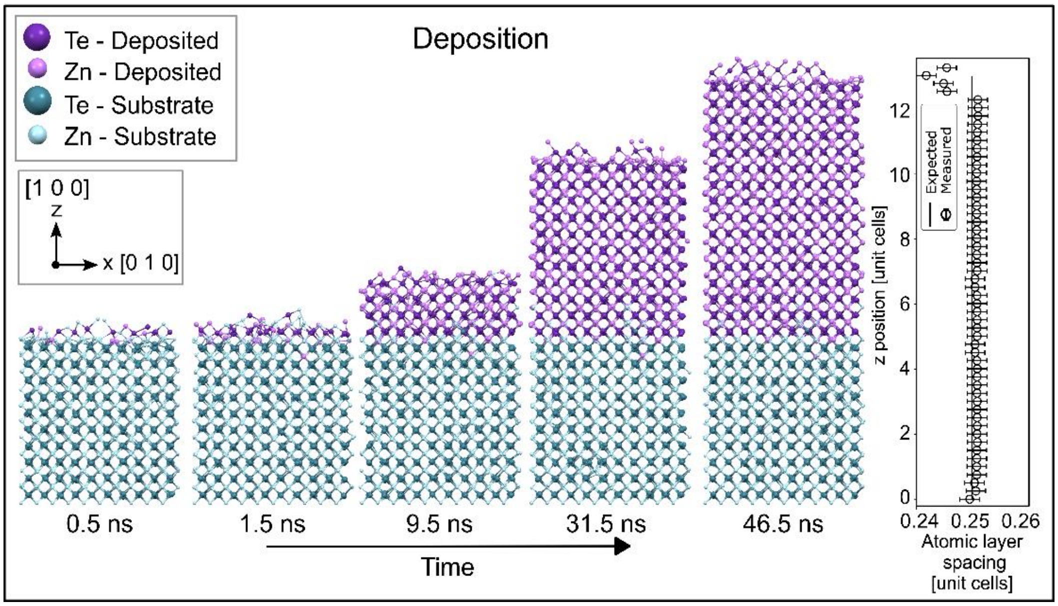

Figure 5. Two dimensional projections of the deposition and growth of a ZnTe film on a lattice matched ZnTe substrate obtained from MD simulations. The lattice constant is 6.150 Å. During deposition, the substrate temperature is 1200 K. Single Zn and Te atoms are deposited at 55 ps intervals with an incident angle of 0° and an incident energy of 5.3

eV - 6.0 eV. Figure reproduced from the supplementary material in [1], with the permission of AIP Publishing.

2.2.5. Measuring thermal conduction of the deposited thin films

The conductivity is calculated from $\kappa = J\left(\frac{dT}{dz}\right)^{-1}$. The heat flux is set or obtained from the set temperature of the heat source/sink, while the temperature profile per atomic layer is computed by binning the atoms of each atomic layer along the z-axis. The parameters are averaged over 100 ps from data recorded every 0.5 fs; these values are then used for further time-averaging. For the temperature profile, averaging is over 40 ns during the non-equilibrium simulation step.

To reduce the influence of Cd impurities and isolate the role of strain caused by heteroepitaxy, values of κ for the deposited ZnTe films are evaluated over regions that are essentially Cd free; with no correlation between the insignificant Cd impurity (a maximum of 2 Cd atoms per region) and the value of κ.

2.2.6 Measuring the potential energy profile

The potential energy per atomic layer is computed by binning the atoms of each atomic layer along the z-axis. The parameters are averaged over 100 ps from data recorded every 0.5 fs; these values are further averaged over the last 5-10 ns of the second equilibration step.

2.2.7. Sensitivity of κ to the simulation duration and the simulation box size

A series of simulations are performed on ZnTe to evaluate the influence of (1) dimensions of the simulation box in the periodic directions, and (2) simulation duration. In these simulations, the ZnTe film is 9 unit cells in the z-direction and varied from 5-18 unit cells in the x- and y-directions. The configuration of the heat source and heat sink is also shown in Figure 6.

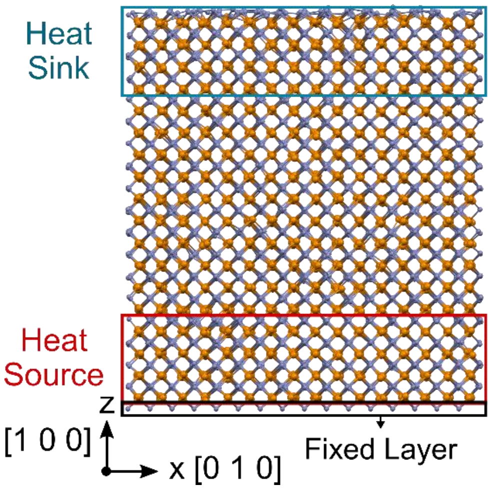

Figure 6. ZnTe film: configuration of the heat source and heat sink for nonequilibrium MD to measure κ. The z-boundaries are fixed in all the reference simulations. The boundaries in the x- and y-directions are periodic and varied to evaluate the influence of the length of the simulation box in the periodic directions. Figure reproduced from the supplementary material in [1], with the permission of AIP Publishing.

2.2.7.1. Size of the simulation box

The dimensions of the simulation box are varied in both the x and y direction but the measured values of κ, presented in Table 2, remain unaltered. Thus, for computational efficiency, the 5×5 cross-sectional area is used for all the simulations in this chapter.

Table 2. Influence of the size of the periodic dimensions on the conductivities of reference samples. The heat source is at 1030 K and the heat sink is at 970 K. Each unit cell is 6.150 Å. Table modified from the supplementary material in [1], with the permission of AIP Publishing.

Simulation box size ($\mathbf{x} \times \mathbf{y} \times \mathbf{z}$)	**$\boldsymbol{\kappa}$ [$\mathrm{Wm^{-1}K^{-1}}$]**
5×5×9	0.87 ± 0.02
8×8×9	0.86 ± 0.02
18×18×9	0.87 ± 0.02

2.2.7.2. Time length of simulation

The temperature and heat flux measurements are binned into consecutive intervals Δt where 1ns ≤ Δt ≤ 40ns. The average temperature and linear fit for the heat flux is determined in each interval and used to measure the corresponding κ, as shown in Figure 7.

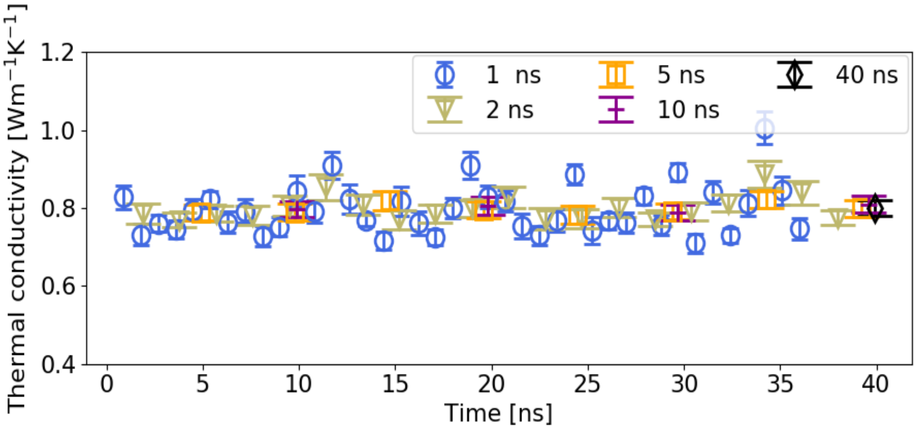

Figure 7. Thermal conductivity of a ZnTe thin film computed over the specified time intervals. Figure reproduced from the supplementary material in [1], with the permission of AIP Publishing.

When bracketing the data into time frames of 5 ns or longer, κ converges to its time averaged value computed over 40 ns. All non-equilibrium MD simulations are performed over 40 ns[1] which should be sufficient to measure steady values of κ.

2.2.8. Calculating the phonon density of states

The vibrational spectrum is computed by[50]

$$I(\omega) = \sum_{n=0}^{N} m_n \int e^{i\omega t} \langle \mathbf{v}_n(t+\tau)\mathbf{v}_n(\tau) \rangle_\tau dt, \qquad \text{(Eq. 9)}$$

and is normalized to its maximum intensity. The $\langle\rangle$ brackets indicate averaging of the correlation function over trajectories of different starting times τ, ω denotes the angular frequency, N is the total number of atoms, and m is the mass of the n$^{\text{th}}$ atom. Since the data is both finite and discrete, the above equation cannot be directly calculated. Considerations must be given to reduce artifacts that arise from the discrete nature of the data. A thorough proof and description of how to implement Eq. 9 is provided in reference [50]. Our method is similar and only differs in the choice of the smoothing window[51] as described below [1]:

1. The velocity-velocity autocorrelation function for each atom is computed:[50]

$$R_n(l\Delta t + \tau) = \frac{1}{L-l} \sum_{i=0}^{L-l-1} \mathbf{v}_{n,i} \mathbf{v}_{n,i+l} \;, \qquad l = 0, .., L-1 \qquad \text{(Eq. 10)}$$

where R_n denotes the mass-weighted velocity ($\mathbf{v}_\text{n}$) autocorrelation of the n$^{\text{th}}$ atom at time $t = l\Delta t + \tau$. L is the total number of time steps.

---

[1] The only exception is the 18 ×18 ×9 unit cell reference simulation which is done over 24 ns because of its extensive computational requirements.

2. The data is mirrored.[50] The output from step 1 is appended in reverse order to itself;

$$R_n(l\Delta t + \tau) = R_n(-l\Delta t + \tau) \qquad \text{(Eq. 11)}$$

3. The data is padded with zeros.[50], [52] An array of zeros is appended to both ends of the output from step 2. We appended an array of zeros that is seven times the length of our output.

4. A hamming window is applied.[51],[50] Let p denote the index of the discrete array formed by R_n at various points in time, then,

$$R_{n,p\_smoothed} = R_{n,p}(0.54 + 0.46 * cos\left(\frac{2\pi p}{P}\right)), \qquad \text{(Eq. 12)}$$

where $|p| < \frac{P-1}{2}$ and P is the length of the array R_n.

5. The fast Fourier transform (FFT) of R_n is computed and multiplied by its complex conjugate. This step is performed using Python's built-in functions for which algorithms are provided in detail.[53],[54]

6. The FFT for all the atoms are summed.

7. The data is normalized to the maximum FFT value.

2.3. Results and Discussion

The simulations can be summarized as follows. The substrate is $Cd_{1-q}Zn_qTe$ where heat transfer is evaluated for two extreme cases when $q = 0$ and $q = 1$. The corresponding change in the relative conductivity k/k_o, where the subscript o refers to the unstrained value, decreases from 1 (unstrained) to ~ 0.65 (strained). Although not explicitly evaluated here, in principle this value can be tuned by changing *q* between 0 and 1. For *q* = 0, ZnTe exhibits ~ 7% uniaxial out-of-plane compressive strain and ~ 6% biaxial in-plane tensile strain which leads to an overall volumetric increase in the heteroepitaxial ZnTe films, see Table 3.

Table 3: Strain and averaged volume of the unit cell in heteroepitaxially grown ZnTe films (ZnTe on CdTe). The strain is $\epsilon = (l - a)/a$, where l denotes the average lattice spacing of the ZnTe film grown under strain and measured along a particular axis at a specific temperature, and a is the corresponding lattice spacing for the relaxed homoepitaxially grown ZnTe film (ZnTe on ZnTe), at the same temperature. The error for ϵ is ± 0.000 Å which reflects time averaged variations of the lattice constant but does not include systematic errors caused by the potential function. Table modified from the supplementary material in [1], with the permission of AIP Publishing.

T [K]	$\boldsymbol{\epsilon}_{\mathbf{x}}$	$\boldsymbol{\epsilon}_{\mathbf{y}}$	$\boldsymbol{\epsilon}_{\mathbf{z}}$	**strained volume [Å^3]**	**unstrained volume [Å^3]**
700	0.061	0.061	- 0.071	241.2 ± 0.0	230.7 ± 0.0
800	0.061	0.061	- 0.072	241.4 ± 0.1	231.4 ± 0.0
900	0.061	0.061	- 0.073	241.8 ± 0.2	231.9 ± 0.0
1000	0.060	0.060	- 0.074	242.1 ± 0.1	232.6 ± 0.0
1100	0.060	0.060	- 0.075	242.5 ± 0.1	233.2 ± 0.0

Other than strain, deposition also leads to atomic mixing around the substrate-film interface. The temperature profile along the ZnTe-CdTe heterostructure (Figure 8 (b1 and b2)) and the lattice spacing along the *z*-direction (Figure 8 (b3)), both exhibit a transition across the interface. Regions free of Cd atoms display uniform lattice spacing and potential energy per atomic layer. Interfacial mixing also occurs in the ZnTe-ZnTe homostructure (Figure 8 (a2)). However, since identical atoms are being substituted for in this case, their mixing does not alter the atomic layer spacing (Figure 8 (a3)), potential energy per atomic layer (Figure 8 (a4)), or the temperature profile (Figure 8 (a1)).

Zn, Cd, and Te in ZnTe and CdTe, have average potential energies of ~ 2 eV per atom. Since the deposited atoms have an incident energy of 5-6 eV, due to momentum transfer the energetic Zn and Te atoms sputter the surface atoms upon incidence. [55] These ejected atoms are either readsorbed on the surface or deflected away from it. The periodic boundaries in the x- and y-directions and a reflector on the upper z-boundary prevent overall loss of ejected atoms. Hence all the atoms are eventually reincorporated into the film.

This sputtering and reincorporation process explains the slightly asymmetric mixing profile across the interface in Figure 5 and the atomic mixing profiles in Figure 8 (a2) and (b2). It is evident that the atomic species contained in each substrate layer remain intact, except at the interface and within two preceding monolayers. In contrast, several monolayers extending from the interface into the film contain atoms that were previously part of the substrate but have now become mixed with the deposited material. The ZnTe homojunctions also exhibit this asymmetric mixing profile across their interface, which cannot be explained by the diffusivity of Zn and Te in ZnTe alone. The mixed atomic species are mainly Zn or Cd, which is unsurprising since the substrate is either Zn terminated in ZnTe or Cd terminated in CdTe. Furthermore ${}_{30}$Zn and ${}_{48}$Cd are both lighter than ${}_{52}$Te, which increases their sputtering yield. [37]

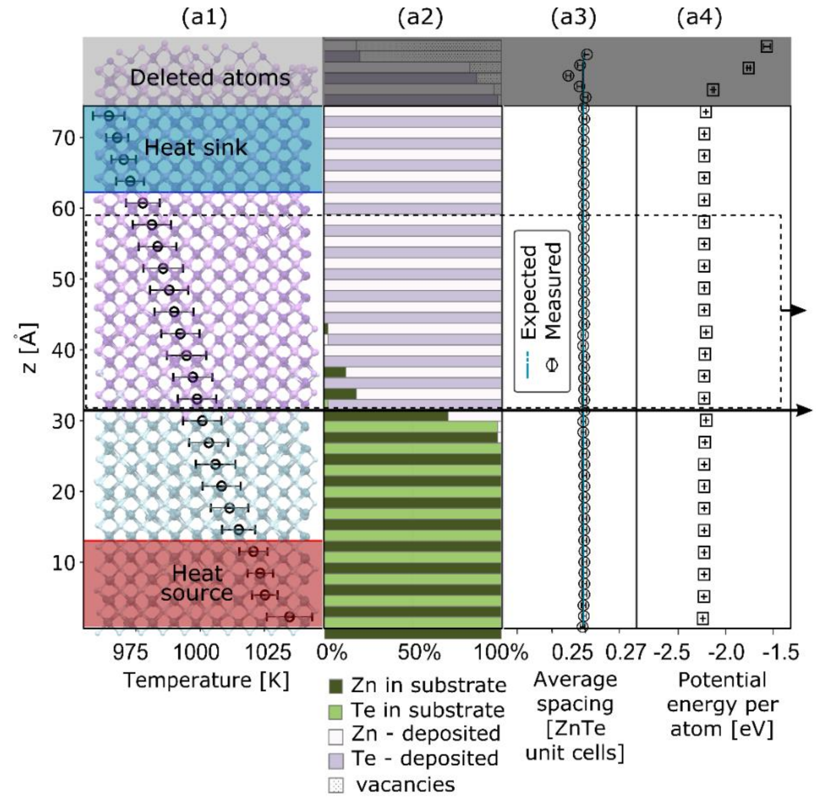

Region used to fit dT/dz for measuring the thermal conductivity of the ZnTe thin film

Substrate surface prior to deposition

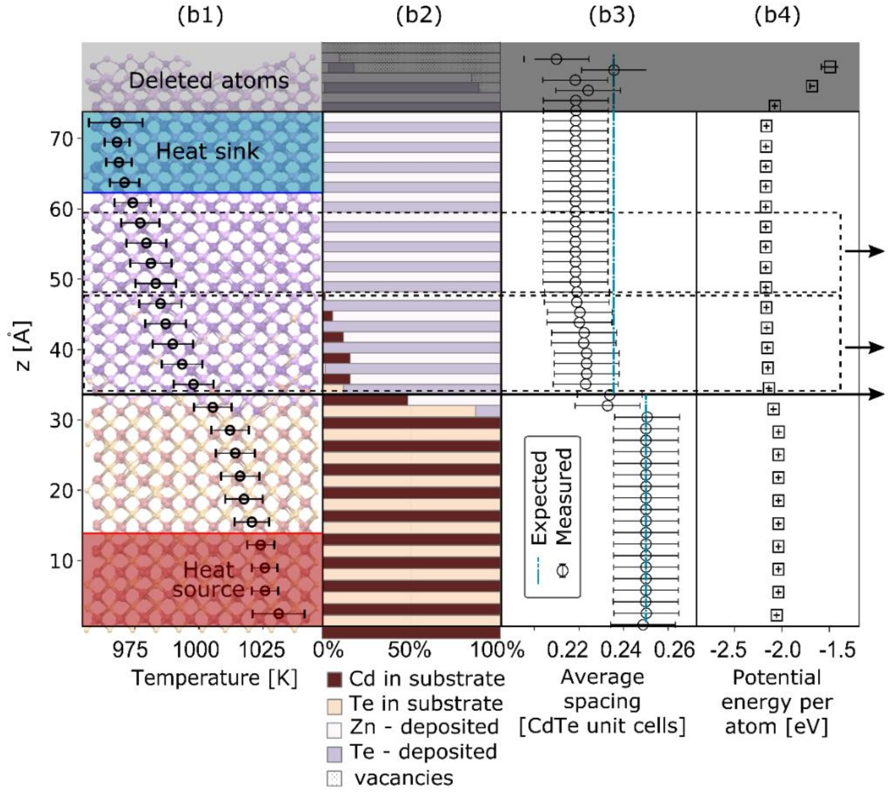

Region used to fit dT/dz for measuring the thermal conductivity of the ZnTe thin film

Transitional region

Substrate surface prior to deposition

Figure 8. (a) Homoepitaxially grown ZnTe structure. (b) Heteroepitaxially grown ZnTe-CdTe structure. (a1) and (b1) show temperature profiles overlaid on the atomic coordinates. Each data point is obtained by time averaging over 40 ns and spatially averaging over two atomic layers that contain a total of 100 atoms. The results in (a2)-(b2) to (a4)-(b4) are evaluated post-deposition and after equilibrating the system for 10 ns at 1000 K. (a2) and (b2) show the atomic species distribution. (a3) and (b3) illustrates the lattice spacing along the z-axis. At 1000 K, the unit cells of ZnTe and CdTe are 6.150 Å and 6.520 Å, respectively. The expected value in the figure is what the lattice spacing would have been if the film and substrate were unstrained and did not mix during deposition. (a4) and (b4) present the potential energy profile. Figure reproduced from [1], with the permission of AIP Publishing.

Experimentally, ZnTe layers grown at 573 K on CdTe have been found to be fully strained up to $\approx 16\ \text{Å}$ [56]. Beyond this thickness, the ZnTe film gradually relaxes and becomes fully relaxed at $\sim 300\ \text{Å}$. This value for critical thickness varies in literature and depends strongly on the growth conditions.[57] While more systematic simulations are required to evaluate the applicability and the limitations of simulating strain and strain-relaxation using molecular dynamics simulations, our results based on strain induced by heteroepitaxy are nonetheless applicable when strain relaxation does not occur. It is worth noting that significant pressure can lead to phase transitions which modulates $\kappa(\epsilon)$. The presented simulations are below the phase transition of ZnTe, which occurs at 9.6 GPa and corresponds to a 9% volume change [58].

Our simulations were designed to systematically identify the role of heteroepitaxial strain on the thermal conductivity of the deposited ZnTe thin films. Hence, in the simulations the sole role of the CdTe substrate during Zn and Te deposition is to act as a template that influences how the deposited Zn and Te atoms are adsorbed and crystalized. In an experiment, the substrate would be of the order of microns or more. However, to reproduce the role of such a substrate during lengthy simulations of material vapor deposition, it is common to only use a few unit cells while keeping the bottom atomic layer fixed.[35],[43] Thus, while the CdTe film induces strain by heteroepitaxy in the deposited ZnTe film , because of its minuscule thickness its properties do not reflect that of an actual substrate.

The thermal conductivity of ZnTe grown on the two different substrates are shown in Figure 9. Heteroepitaxy has reduced thermal conduction and $d\kappa/dT$. To deconvolve the substrate's effect, free standing ZnTe films were simulated, with lattice parameters from the depositions on the two different substrates. These results are also shown in Figure 9. The film deposited on the substrate (case 3 - Figure 9) and the equivalently strained freestanding film (case 4 - Figure 9), both show similar trends and values in thermal conductivity. Since the freestanding film was simulated with diffusive boundaries, this suggests diffuse scattering at the ZnTe-CdTe interface. Simulations of CdTe at larger thicknesses over the temperature range would clarify the contribution of the substrate to thermal conduction and thus the percentage of diffuse scattering at the interface, but remains outside the scope of this work.

In contrast, the thermal conductivity of the freestanding ZnTe is lower than that deposited on ZnTe. This is because the ZnTe-ZnTe interface is coherent, the vibrational modes are not scattered by the interface. Therefore, the additional unit cells from the substrate increase the scattering length and the thermal conductivity of ZnTe. It is important to note that the difference between the freestanding measurements and the deposited ZnTe will depend on the number of unit cells in the substrate so the thermal conductivity will increase with the number of unit cells simulated in the substrate until the bulk thermal conductivity of ZnTe is achieved. Since the thickness of the substrate in the simulation is arbitrary, i.e. the substrate is used as a template for homoepitaxy, the effect of strained-layer heteroepitaxy is best evaluated by comparing the thermal conductivity of the ZnTe film on CdTe with a free-standing ZnTe film of the same thickness. This comparison shows that ZnTe undergoes a 35% reduction in thermal conduction under heteroepitaxial strain.

Strain-induced by heteroepitaxy not only influences the magnitude of $\kappa(T)$ but it also changes $d\kappa(T)/dT$ which is relevant to thermal rectifiers, considered in Chapter 5. At constant pressure $\kappa = \frac{A}{T^{\epsilon}}$ where A is a constant that depends on pressure but not T, and $\epsilon = -\left(\frac{\partial \ln \kappa}{\partial \ln T}\right)_V - 3\alpha T\left(\frac{\partial \ln \kappa}{\partial \ln V}\right)_T$ where α is the thermal expansion coefficient. [19] Linear fits to $\kappa\left(\frac{1}{T}\right)$ are shown in Figure 9. Above the Debye temperature θ_{D}, all the vibrational modes are excited because $k_B T > hf_{\max}$, where k_B is the Boltzmann constant, h is Planck's constant, and $f_{\max}$ is the maximum vibrational frequency. Therefore, most collisions will be Umklapp processes which have a high change in momentum and contribute to thermal resistivity. In this regime the amplitude of the vibrational mode is proportional to T. Since the collision frequency is proportional to the amplitude, $l \propto 1/T$ or $\kappa \propto 1/T$ [4]. Thermal expansion and optic mode scattering may cause $\epsilon > 1$, otherwise, three phonon acoustic-acoustic scattering predicts $\epsilon = 1$. In general, as T increases the scattering length of the vibrations decline and so does thermal conductivity. Another effect to consider is the finite size of the film. If l is comparable to the size of the system, then the dependence on T may diminish. It is worth noting that l is not a constant but is distributed based on the frequency of each mode. Therefore, it is possible to see a T-dependence in κ but the dependence may be skewed by the finite size of the system. The question remaining is why does strain change $d\kappa/dT$? One explanation for the reduced slope with respect to T is that under the observed strain, Umklapp processes decrease, increasing l such that boundary scattering has a more significant effect on κ and so $\left(\frac{d\kappa}{d\epsilon}\right)_{strained} < \left(\frac{d\kappa}{d\epsilon}\right)_{relaxed}$.

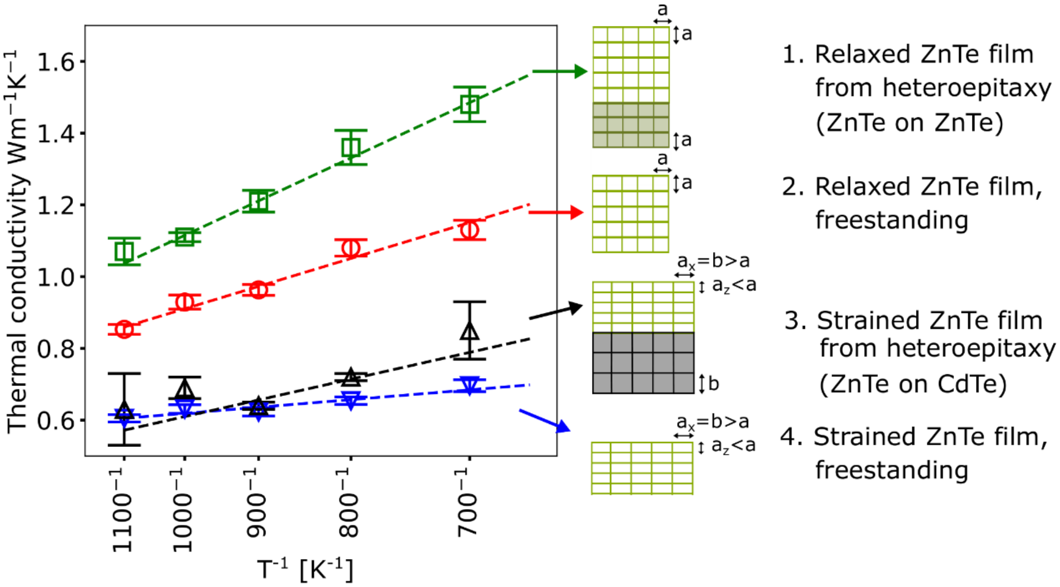

Figure 9: Thermal conductivity of ZnTe under different simulation conditions. The freestanding simulations show the effect of the interface on the thermal conductivity. Case 1 and 3 are reproduced from [1], with the permission of AIP Publishing.

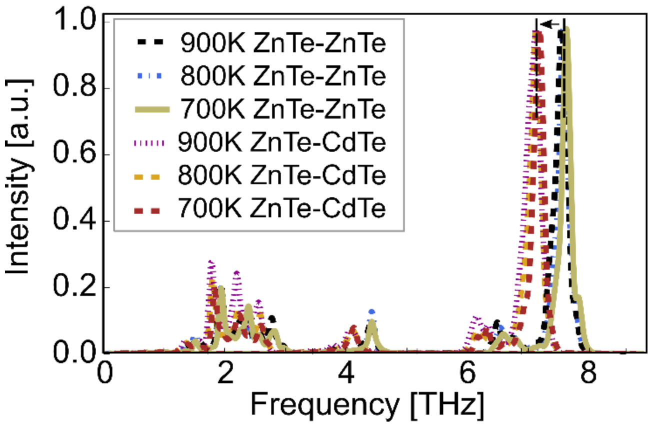

Figure 10. Normalized vibrational density of states spectra for the ZnTe films epitaxially grown on ZnTe, and the heteroepitaxial ZnTe films grown on CdTe. Figure reproduced from [1], with the permission of AIP Publishing.

The vibrational density of states spectra for the ZnTe films grown on both lattice matched and lattice mismatched substrates are presented in Figure 10. Since the system is finite in the $\pm\mathrm{z}$ direction, the local vibrational spectrum depends on the local spatial displacement from the material boundaries. [59] To better isolate the effect of strain, identical regions identified to produce the linear dT/dz fits, highlighted in Figure 8 (b), are compared. The strained ZnTe overlayer exhibits the red shift shown in Figure 10, illustrating softening of the vibrational modes, which is consistent with the reduced κ [60]. The red shift is evident in both the optical and acoustic modes. This suggests that the group velocity, particularly at the Γ point reduces. A reduction in group velocity is often insufficient to deduce behavior in thermal conduction as *aao* or *aaa* scattering may dominate. However, given that the trend in κ with strain is consistent with a reduction in group velocity, suggests that boundary scattering dominates which is consistent with the reduced slope observed in strained $\kappa(T)$, and so thermal conductivity is determined by changes in the group velocity. Using the crude Debye model which assumes linear dispersion, the group velocity is given by $f_{\mathrm{max}}/a_{\mathrm{z}}^{-1}$ so at 1100 °C, $v_{\mathrm{g-relaxed}} = \frac{4.429\times10^{12}}{(6.155\times10^{-10})^{-1}} = 2726$ m/s and , $v_{\mathrm{g-strained}} = \frac{4.107\times10^{12}}{(6.155\times(1-0.075)\times10^{-10})^{-1}} = 2338$ m/s. Therefore, $\frac{v_{\mathrm{g-strained}}\times l_{\mathrm{strained}}}{v_{\mathrm{g-relaxed}}\times l_{\mathrm{relaxed}}} = 0.79$ which is close to the measured $\frac{\kappa_{strained}}{\kappa_{relaxed}} = 0.71$

2.4. Conclusions

The main conclusions from this chapter follow:

1. The reduced magnitude of both $\kappa_{\mathrm{z}}(T)$ and the slope κ_{z}/dT under strain suggest that the intrinsic l for ZnTe increases under biaxial tension and axial (z-direction) compression.

Since the boundaries are diffuse and the film thickness is on the order of l, boundary scattering dominates and trends in $\kappa_z(\epsilon)$ at constant T are consistent with $v_g(\epsilon)$.

2. The ZnTe-ZnTe interface allows for the vibrations to coherently propagate, thus the underlying substrate increases the measured thermal conductivity.

3. Strain induced by heteroepitaxy (ZnTe on CdTe) contributes to 6% biaxial tension and $\sim$ -7.5% axial compression. The thermal conductivity measured along the axial direction decreases by an average of 35% in ZnTe films of 5 unit cell thickness measured between 700 K to 1100 K using the Stillinger-Webber potential.

Chapter 3 includes a systematic study of combined length and strain effects on thermal conduction.

3. Combined Effect of Finite Size and Strain on Thermal Conduction

3.1. Introduction

The combined effect of strain and finite size on thermal conductivity is studied in this chapter. Strain-Engineering of thermal devices requires knowledge of size effects. Two different types of strain are considered, uniform strain, and biaxial strain. Biaxial strain is relevant to thin films as it may be induced by heteroepitaxy or by virtue of thin film processing steps. Given the complexity of biaxial strain, the analysis draws on conclusions made from uniform strain analysis.

3.2. Methods

3.2.1 Measuring thermal conduction

This Chapter uses a modified method for measuring thermal conductivity. It improves the time needed for the system to reach steady-state and is suitable when all the boundaries are periodic. Unlike Chapter 2 where fixed boundaries were used in the z-direction to allow simulating the deposition of ZnTe on a CdTe substrate, in this chapter the thermal conductivity of free standing ZnTe films is assessed under strain without repeating the deposition process, i.e. the coordinates of the atoms are defined during initialization. As such, it is possible to implement all periodic boundaries and implement the methodology explained here.

Figure 11 shows the set up for simulating thermal steady-state in a thin film. All three boundaries of the simulation box shown are periodic and the simulation box is populated with crystalline ZnTe atoms such that z = [1 0 0]. Thermal power is added to atoms within L_{Hot} and equivalently removed from region L_{Cold}. The remaining atoms are left to reach steady state over 50 ns to 63 ns. The temperature profile is averaged and used along with the value of the heat flux to determine κ. The heat source and sink act as perfectly diffuse boundaries that absorbs all incident phonons and re-emits them at a rate depending on the absolute temperature according to the theory of black-body radiation. So, the film is considered finite along the z-direction while it is infinite along the x- and y-directions. To study finite size effects, different film thicknesses of L = {19, 49, 74, 124, 188} unit cells, are simulated at 300 K.

Figure 11. Set up for simulating thermal steady-state in a thin film. All three boundaries of the simulation box are periodic, and the box is populated with crystalline ZnTe atoms such that z = [1 0 0]. Thermal power is added to atoms within L_{Hot} and equivalently removed from region L_{Cold}. The remaining atoms are left to reach steady state.

3.2.2. Extrapolating bulk thermal conductivity

Finite size effects are seen when the distance between the heat source and sink is smaller than the mean free path of the vibrational waves. This size regime where the thermal conductivity is limited by the system size is known as the Casimir limit. Consider an infinite system with a mean free path of l_∞. If the system size is reduced to L, then the average scattering length caused by the boundaries is $L/2$. The reduction in thermal conductivity is caused by the diffuse scattering of elastic waves at the heat source/sink boundary [61].

As explained in Chapter 1, based on the kinetic theory of heat conduction $\kappa = \frac{1}{3}Cv_g l$. Approximating v_g and C as constant,

$$\frac{1}{\kappa} = \left(\frac{1}{3}Cv_g\right)^{-1}\left(\frac{1}{l_\infty} + \frac{1}{l_b}\right) \qquad \text{(Eq. 13)}$$

where $l_b = L/2$ so in the finite dimension, $l = \frac{l_\infty L}{L+2l_\infty}$ and in the limit that $L \to \infty$, $\kappa \to \kappa_\infty$. The y-intercept in the $\frac{1}{\kappa}$ vs. $\frac{1}{L}$ curve gives κ_∞ and the slope gives $2\left(\frac{1}{3}Cv_g\right)^{-1}$. The presented classical simulations can use the Dulong and Petite model for heat capacity, $C = 3k_B n$, where k_B is the Boltzmann constant and n is number density, which results in a heat capacity of 259 $JK^{-1}kg^{-1}$ near its measured value of 264 $JK^{-1}kg^{-1}$ [62]. However, we only consider C from modes that contribute to thermal conduction which is presumably by the acoustic modes and is $\frac{3}{2}k_B n$, so

$$\frac{d\left(\frac{1}{\kappa}\right)}{d\left(\frac{1}{L}\right)} = \frac{a^3}{2k_B v_g} \qquad \text{(Eq.14)}$$

Based on this method we can extrapolate bulk v_g, κ_∞, and l_∞, from measurements taken on various film thicknesses. The extrapolated [63] thermal conductivity for a cross-sectional area of 4×4 [(unit cells)^2] is 19 ± 1 $Wm^{-1}K^{-1}$ and for 12×12 [(unit cells)^2] it is 18 ± 2 $Wm^{-1}K^{-1}$, in agreement with the experimentally measured value of 18 $Wm^{-1}K^{-1}$ for ZnTe [41]. The y-intercept in Figure 12 is the inverse of bulk κ_{ZnTe}.

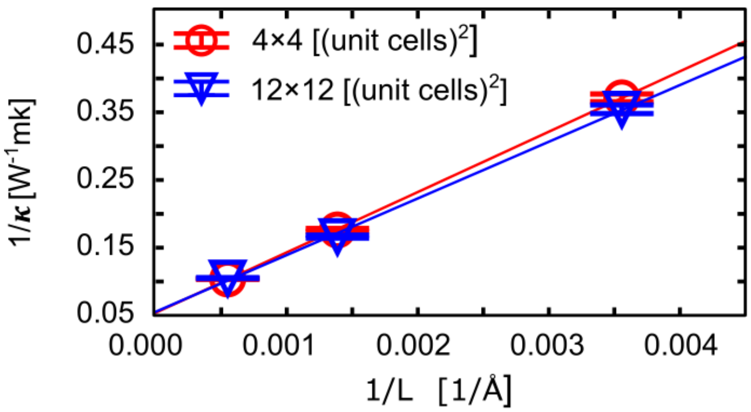

Figure 12. Size dependence of $\frac{1}{\kappa}$ on $\frac{1}{L}$ for two cross-sectional areas of 4×4 and 12×12 [(unit cells)^2]. The linear fits allow the extrapolation of κ_{ZnTe} when $L \to \infty$. Each unit cell is 6.112 Å at 300 K. Figure reproduced from the supplementary material in [1], with the permission of AIP Publishing.

3.2.3. Dispersion of thermal waves

The dispersion curves were measured directly from the MD simulations based on algorithms developed by Kong and his auxiliary post processing code [64]. This method accounts for atomic coordinates in time and uses the fluctuation and dissipation theorem to construct the dynamical matrix. The force constant matrices are obtained from the dynamical matrix and are used to construct the dispersion curve. Sufficiently long measurements result in coefficients that are the “ensemble’s” average. This method works on all - periodic boundaries (i.e. bulk systems) that are well below their melting temperature. The simulation box used is $8 \times 8 \times 8$ unit cells, with 0.003ps time steps, and 100 ns of time averaging. The outputs were smoothed using a signal processing filter in Scipy. [65]

3.3. Results and Discussion

3.3.1. Uniform strain

Figure 13 overlays the temperature profiles of unstrained ZnTe for effective thicknesses, i.e. distance from heat source edge to heat sink edge, of 1149 Å and 452 Å. The reduction of thermal conductivity with film thickness is clear since $\kappa \propto J\left(\frac{dT}{dz}\right)^{-1}$, J is constant, and $\left(\frac{dT}{dz}\right)_{z=115\ \mathrm{nm}} < \left(\frac{dT}{dz}\right)_{z=45\ \mathrm{nm}}$.

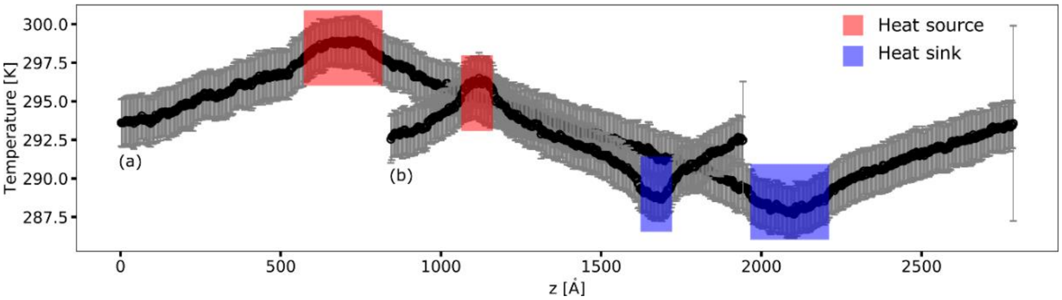

Figure 13: The temperature profiles for unstrained ZnTe of thickness (a) 1149 Å equal to 188 unit cells and (b) 452 Å equal to 74 unit cells, are shown. The center of the heat source and sink are positioned at ¼ and ¾ of the total thickness. The heat flux is fixed by supplying and deducting 0.094 eV/ps to the heat source and sink respectively. Since the boundaries are periodic the heat flux was divided by two in calculations of thermal conductivity. The power was kept constant but the gradient of temperature changes as a function of length scale.

Uniform strain of -3%, 0%, +3% is applied along the x-, y-, z-direction by respectively setting the lattice spacing to $0.97a_0$, a_0, and $1.03a_0$ where $a_0 = 6.112$ Å is the equilibrium lattice spacing for ZnTe determined from NPT simulations at 300 K; see

Chapter 2. Figure 14 shows the effect of strain on the temperature profile of a 452 Å film. A power of 0.094 eV/ps is added and deducted from the heat source and sink respectively. Under compression, the material becomes more thermally resistive and imposes a higher temperature gradient, while expansion has minimal effect at this film thickness.

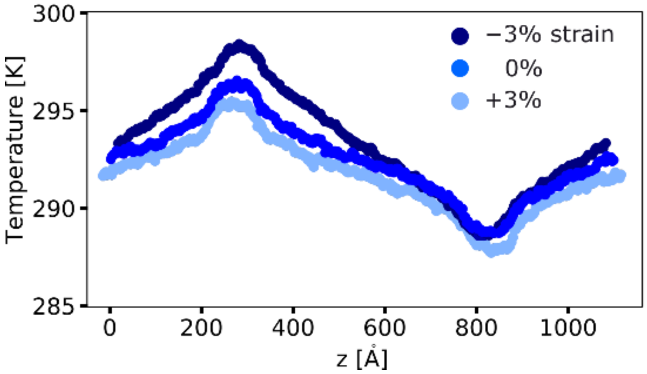

Figure 14: Temperature profile of ZnTe under different uniform strains defined by $(L - L_0)/L_0$. The heat source generates 0.094 eV/ps while the heat sink absorbed the same amount. The distance between the source and sink is 452 Å equal to 74 unit cells. To improve readability, error bars are not presented in this graph.

The combined effects of both strain and film thickness are captured in Figure 15. To complement this data phonon dispersion curves for bulk ZnTe are calculated and shown in Figure 16. As the material compresses, κ_{ZnTe} lessens. This is true for all thicknesses. However, under tension the trend of κ with strain is thickness dependent.

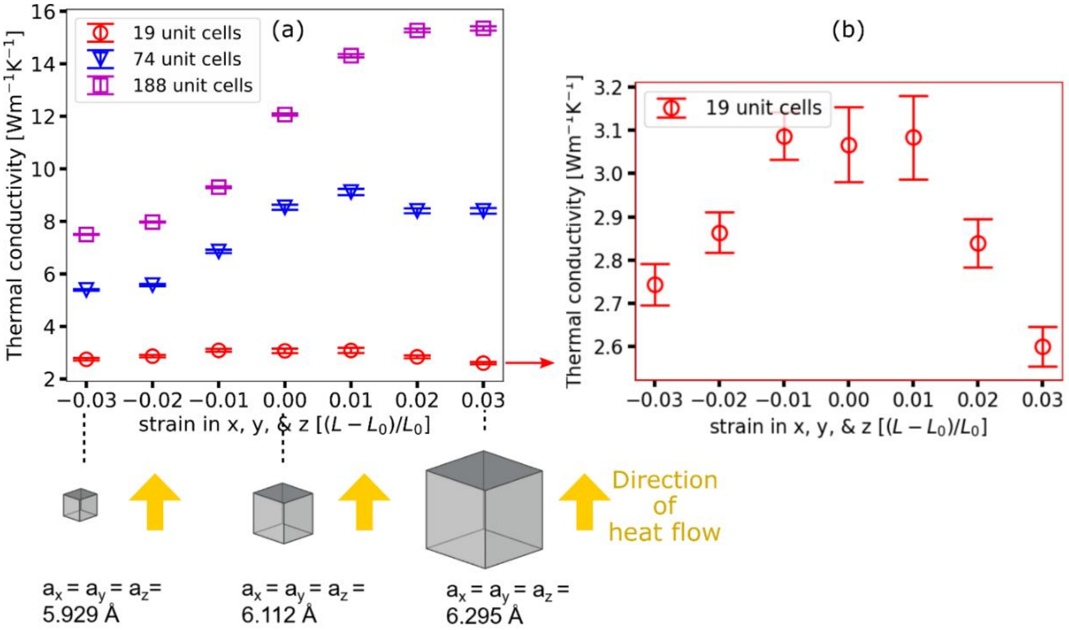

Figure 15: (a) Effect of uniform strain on the thermal conductivity of ZnTe. The boundaries in the x- and y-direction are periodic while it is finite and completely diffuse in the z-direction. The thermal conductivity is measured along the z-direction for various lengths. Each unit cell is 6.112×(1+strain) [Å].

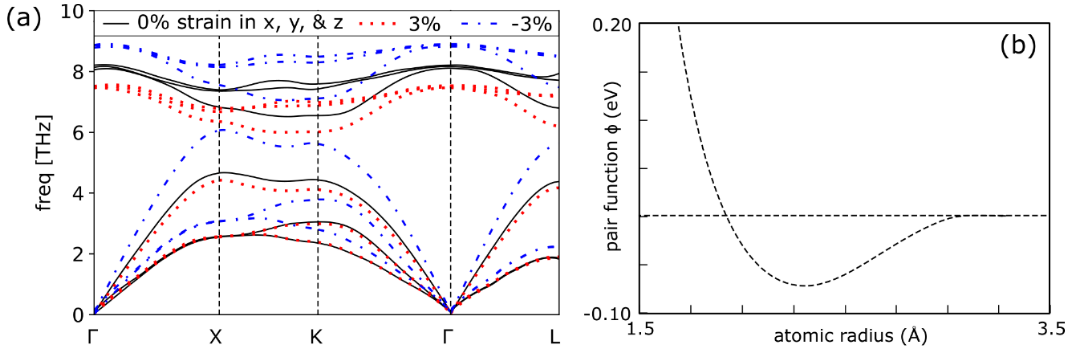

Figure 16: (a) Comparison of ZnTe dispersion curves at three different strains, along different symmetry directions of the Brillouin zone. The strain is applied uniformly along the x-, y-, and z-directions. (b) The pair function of an Stillinger-Weber potential [43].

Under compression, the energy of the optical modes and acoustic modes increases while under tension it either declines or remains unchanged. The energy increase under compression is expected; as the lattice spacing shrinks, the number of modes per unit volume increases and so does the maximum energy of the vibrational modes, while under tension the opposite occurs. The asymmetry in the magnitude of the change may arise from the asymmetry inherent to the interatomic function. The bulk modulus is approximately given by $B = a\left(\frac{\partial^2\Phi}{\partial r^2}\right)_{r=a}$, since $\left|\frac{\partial^2\Phi}{\partial r^2}\right|_{\mathrm{a<a_0}} > \left|\frac{\partial^2\Phi}{\partial r^2}\right|_{\mathrm{a>a_0}}$ and B is also proportional to the slope of LA modes at the Γ point, then one would expect a greater change in dispersion of LA modes under compression than tension.

The contribution of acoustic modes to thermal conduction is of interest and cannot be deduced by only considering the group velocity at the Γ point. The fraction of all acoustic phonons that carry heat in the [100] direction is described and is implemented in similar way along all the other directions.[20]

$$F = \left(\frac{q_c}{\bar{q}_{\max}}\right)^3 \tag{Eq.15}$$

where

$$q_{\max}([100]) = 2\pi/a_0 \tag{Eq.16}$$

is the wavelength of the wavevector that extends from the center to the edge of the first Brillouin zone in the [100] direction, a_0 is the lattice constant of the crystal,

$$\bar{q}_{\max} = \left(\frac{3}{\pi}\right)^{\frac{1}{3}} q_{\max}([100]) \tag{Eq.17}$$

is the average radius of the first Brillouin zone,

$$q_c = 2\pi/\lambda_c \tag{Eq.18}$$

is the cutoff wavevector at the cutoff wavelength λ_c,

$$\lambda_c = v_g/\nu_{\max} \tag{Eq. 19}$$

and $\nu_{\max}$ is the maximum frequency. Shorter wavelengths can be assumed to have zero propagation velocity. This is because near the zone center, the phonons' velocity rapidly drops and deviates from the approximate v_g.

It is important to note that the calculations below are best estimates of the group velocity at the Γ point as the exact value would require very large simulation cells and time averaging.

Table 4: Effect of strain on v_g at the Γ point and the estimated contribution of the acoustic modes to thermal conduction for each polarization along the [010], [011], and [111] crystallographic directions. The estimated error in the acoustic v_g is 1.1E+02 m/s, in the longitudinal v_g is 1.5E+01 m/s, and in F is 0.05. This error is the standard deviation of the acoustic modes or longitudinal modes along the symmetric [001], [010], and [100] directions.

		v_g [m/s]			F		
Strain		– 3 %	0 %	+3 %	– 3 %	0 %	+3 %
[010]	TA1	2.62E+03	2.10E+03	2.27E+03	0.35	0.43	0.37
	TA2	2.80E+03	2.38E+03	2.44E+03	0.29	0.30	0.30
	LA	4.90E+03	3.88E+03	3.71E+03	0.42	0.41	0.44
[011]	TA1	2.13E+03	1.85E+03	1.98E+03	0.43	0.42	0.40
	TA2	2.81E+03	2.34E+03	2.45E+03	0.46	0.45	0.40
	LA	4.99E+03	3.95E+03	3.87E+03	0.27	0.29	0.27
[111]	TA1	2.48E+03	2.10E+03	2.13E+03	0.25	0.26	0.28
	TA2	2.52E+03	2.16E+03	2.38E+03	0.24	0.25	0.21
	LA	5.20E+03	4.21E+03	4.10E+03	0.42	0.41	0.43
average T1 & T2		2.56E+03	2.16E+03	2.27E+03	0.33	0.35	0.33
average L		5.03E+03	4.01E+03	3.90E+03	0.37	0.37	0.38
average T & L		3.38E+03	2.78E+03	2.81E+03	0.35	0.36	0.34

Table 4 shows that the fractional contribution of the acoustic modes, at various strains, are within 2%, but the average v_g increases by 26% under compression, with little change under expansion. Not taking scattering into account, one would expect the 188 unit cell film to show an increase in thermal conduction under compression and no significant change under expansion. Since this is not the case, scattering can explain the evident trends.

Using Eq. 11 and Eq. 12 the average bulk scattering length and thermal conductivity is shown in Figure 17. Anharmonic scattering can justify the trends in thermal conduction under strain. Though the methodology is crude, as it does not measure the scattering length of each participating mode, nor does it account for the distribution of the scattering length, it is still informative in showing the dominance of vibrational scattering on the thermal conduction.

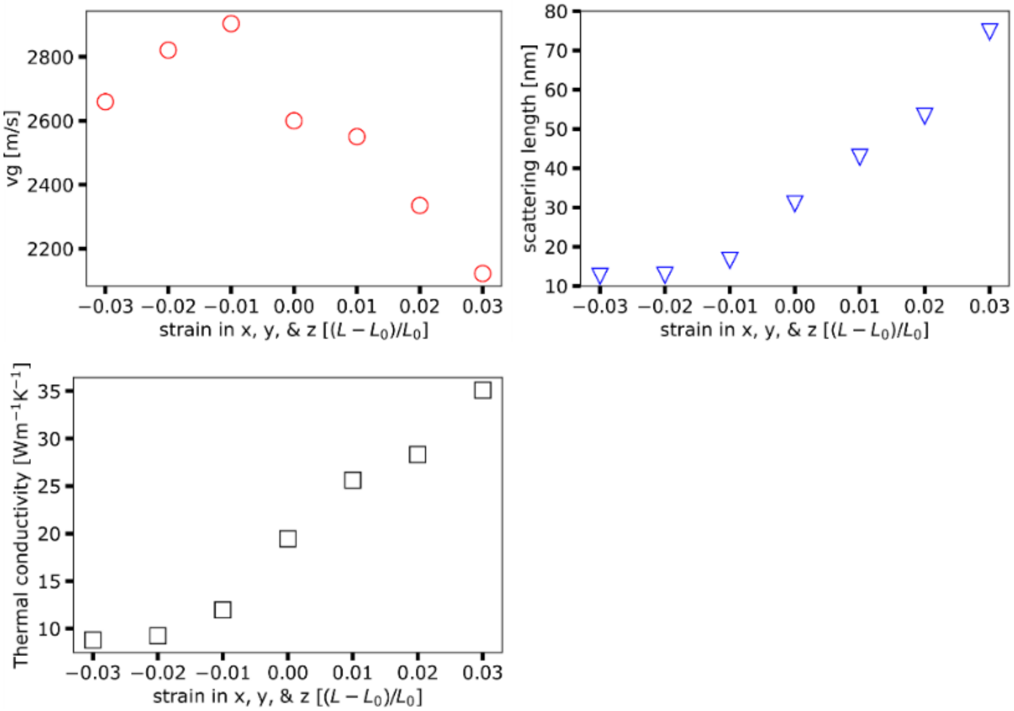

Figure 17: Extrapolated values for average group velocity, scattering length, and thermal conductivity for bulk ZnTe.

Under compression, $\frac{d\kappa}{d|\epsilon|} < 0$ for all three film thicknesses of 19, 74, and 188 unit cells. Since this behavior is in contrast with the increase of $\langle v_g \rangle$ under compression, it suggests that scattering increases and reduces l. As the thickness becomes smaller, $|\frac{d\kappa}{d\epsilon}|$ reduces, suggesting that the scattering length is comparable to the thickness, especially at 19 unit cells. Under tensile strain the sign of $\frac{d\kappa}{d\epsilon}$ depends on the thickness of the film. At 188 unit cells $\frac{d\kappa}{d\epsilon} > 0$, at 74 unit cells $\frac{d\kappa}{d\epsilon} \approx 0$ and at 19 unit cells $\frac{d\kappa}{d\epsilon} < 0$. The increased l under tension, combined with the decline in κ at 19 unit cells, suggests that the thermal conductivity is limited by the thickness of the film so that the reduced group velocity dictates the evident trends. This observation is consistent with the results in Chapter 2.

3.3.2. Biaxial strain

The material was placed under biaxial strain in the x- and y-direction as shown in Figure 18. In (a) the film is terminated along z and the thermal conductivity is measured along the z-direction. In (b) the film is terminated along x and thermal conductivity is measured along x-direction. In practice, case (a) may be realized in heteroepitaxy while the 188 unit cell structure in case (b) may depict the in-plane thermal conduction for case (a).

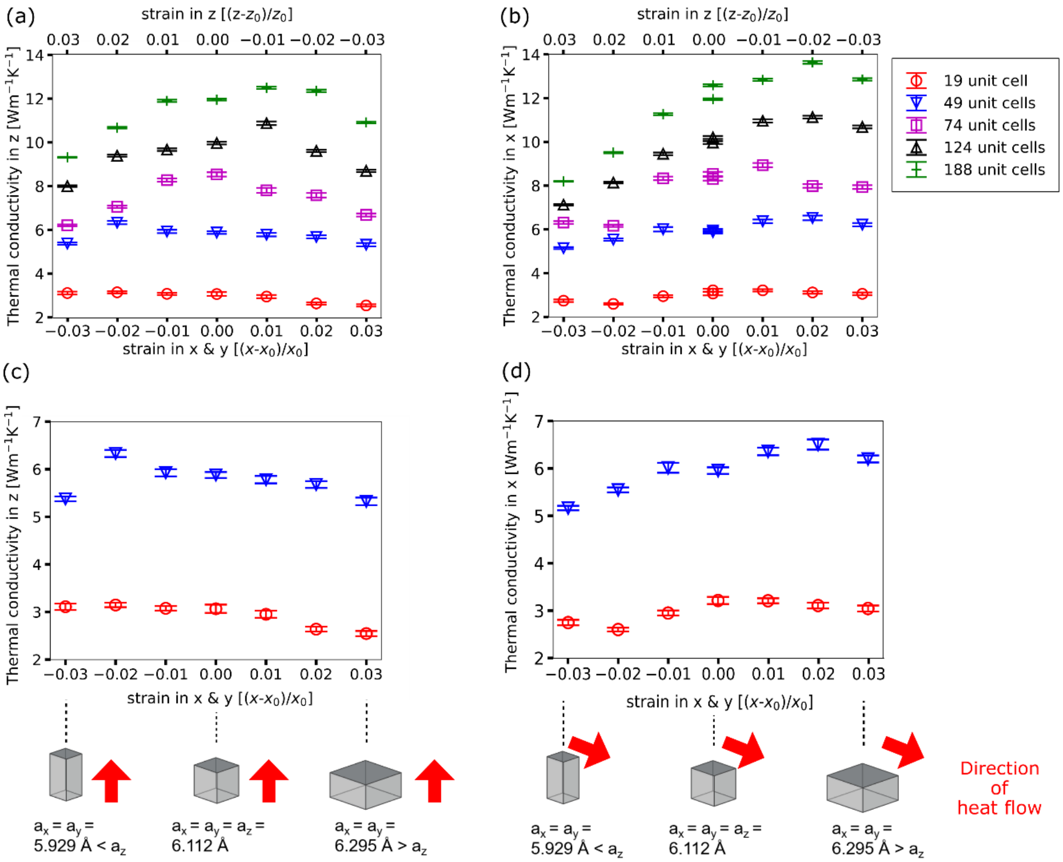

Figure 18: (a) thermal conductivity along the z-direction and (b) thermal conductivity along the x-direction for films under biaxial x and y strain and relaxed in the z-direction. The thickness of the film, dictated by the distance between the heat source and sink, is given on the right. Each unit cell is $6.112 \times (1 + \mathrm{strain})$.(c) and (d) magnify the results for the 19 and 46 unit cell films from (a) and (b) respectively.

The dispersion curves are shown in Figure 19. Like uniform strain, under compression the number of nodes per unit length increases which increases the number of modes and the energy they carry causing an upward shift of the energy of the modes. Tension is the opposite. Also, the bulk dispersion curve shows a larger response to compression than to tension due to the asymmetry of the potential function about the minimum.

Since biaxial x and y strain breaks the cubic symmetry of the crystal, the dispersion along the <100> vectors are nonequivalent as seen in Figure 19(b). The vibrations are influenced by all the atoms in the system, so the in-plane biaxial tension (compression) and the out-of-plane axial compression (tension) will have opposing effects on the dispersion. Overall, this reduces the changes caused by strain which is evident by comparing **Error! Reference source not found.**(a) with Figure 16. Note that the x-axis of the dispersion curve is normalized to the distance between the two boundaries, ex. $\Gamma\mathrm{X}$, so v_g is the slope of the dispersion curve multiplied by the distance.

Table 5 shows v_g of each mode. The -3% strain in x and y increases $v_{g,\mathrm{x,y}}$ by $\sim +8\%$ while κ_{x} drops by 33% . The mismatch between trends in v_g and κ suggests that Umklapp scattering is responsible for the evident trends under biaxial compression. This holds for all the studied thicknesses like what was seen for uniform compression. Under biaxial tension, in general, when the films are thick enough so that Umklapp scattering dominates, $\kappa_{\mathrm{x,y}}$ increases suggesting a decrease in Umpklapp scattering. As the film thins, boundary scattering dominates and reduces κ_{x}. At 19 unit cells, κ_{x} follows trends in $v_{g,\mathrm{x}}(\epsilon)$ under tension. Note that for biaxial tension, for a given film thickness $d\kappa_{\mathrm{x,y}}/d\epsilon$ may switch from positive to negative. This may be a consequence of bond angle changes induced by biaxial strain.

The influence of biaxial x and y strain on κ_{z} is more complicated as the competing effects of the opposing x-y vs z strain are more prominent. When Umklapp scattering dominates (at 188, 124, and 74 unit cells), $\kappa_{\mathrm{z}}(\epsilon)$ follows the general shape of $\kappa_{\mathrm{x}}(\epsilon)$. As the film thins and boundary scattering dominates (49 and 19 unit cells), $\kappa_{\mathrm{z}}(\epsilon)$ seems to mirror $\kappa_{\mathrm{x}}(\epsilon)$.

One explanation follows; when the film is thinned boundary scattering dominates for both tension and compression. As such, the shape for $\kappa_{\mathrm{z}}(\epsilon)$ follows $v_{g,\mathrm{z}}(\epsilon)$. This is different than $\kappa_{\mathrm{x,y}}$ in biaxial strain or $\kappa_{\mathrm{x,y,z}}$ in uniform strain since in those two cases, thermal conductivity under compression was still affected by increased Umklapp scattering.

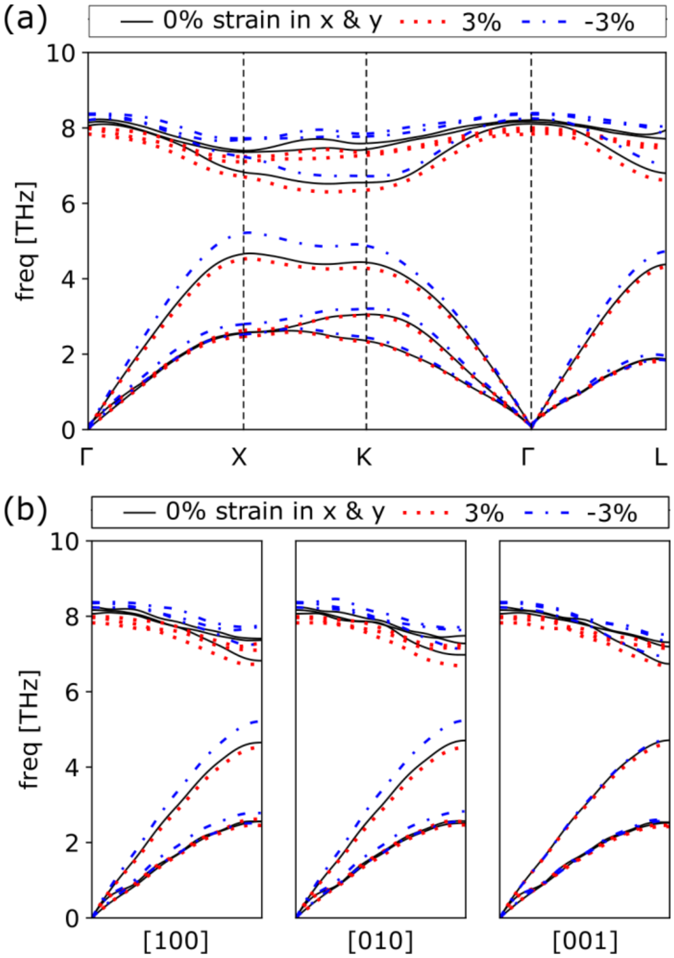

Figure 19: (a) Comparison of bulk ZnTe dispersion curves at three different biaxial strains, along different symmetry directions of the Brillouin zone. The strain is applied uniformly along the x, y, direction while it is relaxed in the z direction. (b) Biaxial strain breaks the cubic symmetry of the crystal and the <100> dispersion curves.

Table 5: Effect of strain on the group velocity v_g at the Γ point along the [100], [010], and [001] crystallographic directions. The estimated error in the acoustic v_g is 1.1E+02 m/s and in the longitudinal v_g is 1.5E+01 m/s which is the standard deviation of the acoustic modes or longitudinal modes along the symmetric [001], [010], and [100] directions of an unstrained ZnTe crystal.

	$v_{\mathbf{x}=[100]}$ [m/s]			$v_{\mathbf{y}=[010]}$ [m/s]			$v_{\mathbf{z}=[001]}$ [m/s]		
ϵ in x&y	– 3 %	0 %	+3 %	– 3 %	0 %	+3 %	– 3 %	0 %	+3 %
avg. T1&T2	2370	2240	2300	2370	2270	2320	2390	2280	2230
LA	4220	3880	3900	4240	3890	3910	3990	3910	3750
avg. T&L	3300	3060	3100	3310	3080	3120	3190	3100	2990

3.4. Conclusions

Increasing uniform compression in the x-, y-, and z-directions reduces κ for thin films. Since v_g increases with increasing compression, this decline in κ is associated with increased Umklapp scattering. As the film becomes thinner, boundary scattering prevails and consequently κ becomes less sensitive to ϵ. In contrast, under uniform expansion, Umklapp scattering decreases. Here, for thicker films dominated by Umklapp scattering κ increases, but as the film is made thinner and boundary scattering dominates, κ declines in magnitude while $d\kappa/d\epsilon$ depends on the balance between boundary and Umklapp scattering. For sufficiently thin films where boundary scattering dominates, e.g., those composed of 19 unit cells, κ depends primarily on $v_g(\epsilon)$ during uniform expansion.

Biaxial strain in x and y breaks the cubic symmetry of the crystal. Since the crystal can relax in the z-direction, it compresses under biaxial tension and dilates under biaxial compression. The competing effects in the x-, y- and z-directions reduce the overall changes caused by strain. Similar to the behavior for uniform strain, $\kappa_{\mathrm{x,y}}$ also declines under biaxial compression despite the increase in $v_{g,\mathrm{x,y}}$, suggesting an increase in Umklapp scattering that impacts even the thinnest 19 unit cell thick film. For thicker films under biaxial tension, $\kappa_{\mathrm{x,y}}$ increases when Umklapp scattering dominates, suggesting a decrease in Umklapp scattering. Conversely, as the film thins, boundary scattering dominates and reduces κ_{x}. For the 19 unit cell thin film, κ_{x} follows the behavior of $v_g(\epsilon)$. For any film thickness, under biaxial tension $d\kappa_{\mathrm{x,y}}/d\epsilon$ can switch from positive to negative, which may be attributed to the change in bond angle induced by biaxial strain. The extent of this effect requires further study and is recommended for future work.

Biaxial strain in the z-direction is more complex as the competing effects of the opposing x, y vs z strain become more prominent. When Umklapp scattering dominates, $\kappa_{\mathrm{z}}(\epsilon)$ follows the general trend of $\kappa_{\mathrm{x}}(\epsilon)$. As the film thins and boundary scattering dominates, $\kappa_{\mathrm{z}}(\epsilon)$ mirrors $\kappa_{\mathrm{x}}(\epsilon)$. A conjecture is that, as the film is sufficiently thinned, boundary scattering dominates for both tension and compression so that variations in $\kappa_{\mathrm{z}}(\epsilon)$ follow those in $v_{g,\mathrm{z}}(\epsilon)$. This is different from the behavior of $\kappa_{\mathrm{x,y}}$ during biaxial strain or $\kappa_{\mathrm{x,y,z}}$ under uniform strain since, for those two cases, thermal conductivity under compression is still influenced by an increase in Umklapp scattering.

The results in this chapter provide an understanding of $\kappa(\epsilon)$ for thin films based on bulk phonon dispersion and bulk $\kappa(\epsilon)$, independent of the material system and potential function. Further research is suggested to test the generality of these results.

Chapter 4. Considerations of the Stillinger-Webber potential function for future work

The simulations are conducted using LAMMPS [42] and employ the Zn-Cd-Hg-S-Se-Te Stillinger-Weber (SW) potential that appropriately reproduces experimental lattice constants, cohesive energies and elastic constants, while ensuring that the lowest energy structure is tetrahedral.[43] Stillinger-Weber potentials [66] have a term in their potential energy function that penalizes non-tetrahedral bond formation, an important property that allows the potentials to predict the crystalline growth of stoichiometric compounds under stoichiometric growth conditions during MD simulations of vapor deposition.[43]

4.1. Stillinger-Weber formulation

The Stillinger-Weber potential provides the total energy of a system of N atoms as [43]

$$E = \frac{1}{2}\sum_{i=1}^{N}\sum_{j=i_1}^{i_N}[V_{IJ}^{R}(r_{ij}) - V_{IJ}^{A}(r_{ij}) + u_{IJ}(r_{ij}) \times \sum_{\substack{k=i_1 \\ k\neq j}}^{i_N} u_{IK}(r_{ik}) \left(\cos\theta_{jik} + \frac{1}{3}\right)^2] \quad \text{(Eq. 20)}$$

where $i_1, \dots i_N$ is a list of neighbors of atoms i, θ_{jik} is the bond angle formed by atoms j and k at the site of atom i, $V_{IJ}^{R}(r_{ij})$ and $V_{IJ}^{A}(r_{ij})$ respectively are pairwise repulsive and attractive functions, $u_{IJ}(r_{ij})$ is another pair function, where the subscripts ij and IJ respectively indicate the atom pair and the pair species. Furthermore,

$$V_{IJ}^{R}(r) = A_{IJ}\epsilon_{IJ}B_{IJ}\left(\frac{\sigma_{IJ}}{r}\right)^{p} \exp\left(\frac{\sigma_{IJ}}{r-a_{IJ}\sigma_{IJ}}\right), \quad \text{(Eq.21)}$$

$$V_{IJ}^{A}(r) = A_{IJ}\epsilon_{IJ}\left(\frac{\sigma_{IJ}}{r}\right)^{q} \exp\left(\frac{\sigma_{IJ}}{r-a_{IJ}\sigma_{IJ}}\right) \quad \text{(Eq. 22)}$$

and

$$u_{IJ}(r) = \sqrt{\lambda_{IJ}\epsilon_{IJ}}\exp(\frac{\gamma_{IJ}\sigma_{IJ}}{r-a_{IJ}\sigma_{IJ}}). \qquad \text{(Eq.23)}$$

The parameters $\epsilon, \sigma, a,\ A$ and B are fitted based on physical properties including cohesive energy, lattice constant, and bulk moduli, while $p = 4$, $q = 0$, and $\gamma = 1.2$ are fixed. The values for γ and λ are constrained to give the lowest energy for the tetrahedral structure of the compound. They also influence the shear modulus (C'or C_{44}) through their effect on the angular function $u(r_0)$ at the equilibrium bond length r_0. $a\sigma$ represents the interaction range of the potential so that for $r \geq a\sigma$, the functions $V^R(r)$, $V^A(r)$, and $u_{IJ}(r)$ all vanish. The potential is essentially a sum of the pair potentials $V_{IJ}^R(r_{ij}) - V_{IJ}^A(r_{ij})$ and a three-body term $u_{IJ}(r_{ij})u_{IK}(r_{ik})\left(\cos\theta_{jik} + \frac{1}{3}\right)^2$which leads to an energy rise for non-tetrahedral bond formation. This type of potential is particularly useful for simulating thin film deposition. The SW potential used in this thesis [43], was developed to enable high-fidelity and high-efficiency atomistic simulations of defects in Zn, Cd, Te, Se, Hg, and S II-VI semiconducting compounds. Since defect formation is highly dependent on the elastic properties of materials, special attention was given to this.

4.2. Comparison of simulated and experimental properties of ZnTe

Table 6 compares some of ZnTe experimentally measured properties with those obtained from the SW potential used in this thesis. The values are in great agreement with one another. Furthermore the C_{44} modulus which was not explicitly provided in the table was said to be in agreement with experimental results in reference [43].

Table 6. Comparison between experimental properties of ZnTe and those from the SW potential. The calculated values (Cal.) were obtained by the authors in [43] and the experimental values (Exp.) are from the references in [43].

Structure		$\Omega\ [\text{Å}^3/\text{atom}]$		$E_c\ [\text{eV}/\text{atom}]$		$B\ [\text{eV}/\text{Å}^3]$		$C'\ [\text{eV}/\text{Å}^3]$	
Exp.	Model	Exp.	Cal.	Exp.	Cal.	Exp.	Cal.	Exp.	Cal.
zb	zb	28.4	28.4	-2.36	-2.36	0.32	0.32	0.10	0.10

This chapter extends the comparison by considering the thermal wave dispersion curves shown in Figure 20. The experimental dispersion data claimed a nominal error of 0.02 THz with a maximum of 0.1 Hz,[67] which are not illustrated as they are smaller than the size of the markers used in Figure 20. The LA modes agree well with experimental data. TA modes agree in the limit of long wavelengths, i.e. $\Gamma \rightarrow 0$, where the group velocity of the acoustic branches represents the speed of sound in matter. In contrast, the calculated optical modes poorly agree with experiments.

Optical modes are exclusive to crystals with two or more atoms per primitive cell. The atoms vibrate against each other, while their center of mass is fixed. If the atoms are ionic or have some level of ionicity, such vibrations will create electric moments and generate electromagnetic waves. The electromagnetic interactions are long-range forces, while the potential in use, only considers nearest-neighbor interactions so the interaction energies become negligibly small at atomic separations substantially less than the cut-off [43]. It is stipulated that the short-range nature of this potential in combination with the limiting governing physics is what leads to the deviations between experimental and measured optical modes.

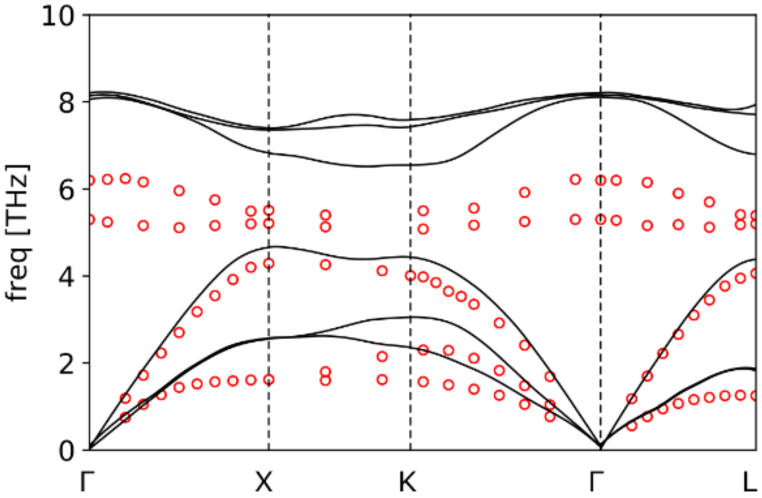

Figure 20: Comparison of experimental dispersion curve shown by open circles [67], and the dispersion curve calculated for ZnTe SW potential [43] along different symmetry directions of the Brillouin zone. The experimental data claimed a nominal error of 0.02 THz with a maximum of 0.1 THz, which are not illustrated as they are smaller than the size of the markers used.

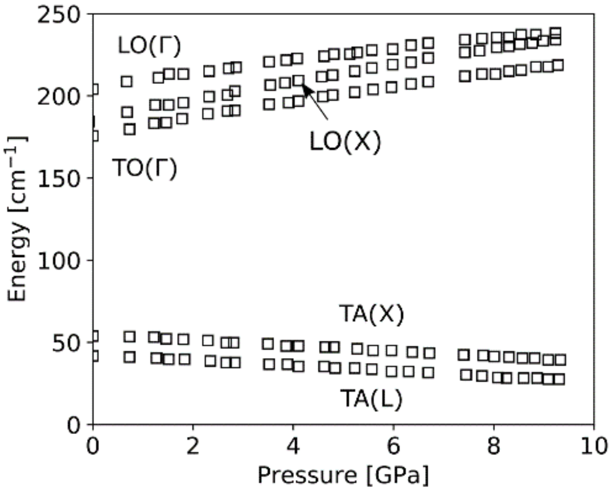

Figure 21. Frequency values derived from experimental Raman frequencies of ZnTe as a function of pressure at 300 K. Image modified from [68].

The two main differences between the measured and experimental dispersion curves in Figure 20 are in the maximum frequency $\nu_{\mathrm{max,TA}}$ and the *a-o* gap. $\nu_{\mathrm{max,TA}}$ is lower in the experimentally measured dispersion, meaning that less of the TA modes contribute to thermal condition. Furthermore, the *ao* gap is also smaller. It is more complicated to deduce how the *a-o* gap affects scattering simply by observing the dispersion curve. Since as explained in Chapter 1, *aao* increases as the *ao* gap widens until the gap becomes so large that no two acoustic modes can combine to reach the optical modes [2]. In any case, the *a-o* gap would affect scattering rates and so the simulated and experimental results would deviate.

Figure 21 shows the effect of strain calculated from Raman spectra. While the optical modes frequency increases with pressure, the TA mode decreases with pressure. This causes a decrease in stiffness of the modes which is common to most tetrahedral cubic semiconductors and is strongly related to the pressure-induced phase change to the rock-salt structure [22]. This softening is not captured in the ZnTe SW potential and may further result in deviations between experimental measurements of thermal conductivity and those from this study. It is important to note that simulation-based studies on $\kappa(\epsilon)$ or $\kappa(P)$ are commonly conducted without validating the potential function under strain or pressure [24][33][16][60]. This may be due to limitation in available potential functions, challenges in developing new potential functions and limited experimental results for comparison. It is further worth noting that the deviation between MD and experimental thermal wave dispersion is not unique to the potential function used in this thesis. Porter et al. shows that three representative interatomic potential functions for Si – SW, Tersoff, and hybrid – all fail to describe silicon's Grüneisen parameter, i.e. the pressure dependence of the potential function.[69] It is important to validate the Grüneisen parameter of the potential function for any simulation that involves changes in volume or pressure as it effects both qualitative and quantitative results. However, such MD potential functions are scarce. In general, Density Functional Theory (DFT) provides better agreement between experimental and calculated interatomic force constants but is computationally demanding, which limits the size of the systems to typically less than 100 atoms, as such, size dependent studies are difficult or impossible. While molecular dynamics simulations can be driven by forces calculated by density functional theory, like in bond order potentials, this significantly increases the simulation time [9]. Robust interatomic potential intended for thermomechanical behavior of crystals requires attention to fundamental properties such as thermal wave dispersion and the Grüneisen parameter all while allowing computations of representative sized materials. Given the scarcity of such potential functions and their importance to strain engineering in nanostructures, the development of such potential functions is recommended for future work.

Chapter 5. Applications and future work

5.1. Applications to thermal rectifiers

Most sections are reproduced from T. Majdi, et. al., “Recipe for optimizing a solid-state thermal rectifier,” *Int. J. Therm. Sci.*, vol. 117, pp. 260–265, 2017.

5.1.1. Introduction

A thermal rectifier is a device in which the magnitude of the heat flux depends on the sign of the temperature gradient There are several mechanisms that enable thermal rectification. A good review is provided in [70]. This chapter is based on thermal rectification induced by varying the local temperature dependence of thermal conductivity, specifically in a one-dimensional bi-segment steady state system. The theoretical maximum, when thermal conductivity is a linear function of temperature is $R = |J_F/J_R| = 3$, where J_F and J_R respectively denote the heat flux in the forward *F* and reverse *R* directions [71]. The analytical expression for R is expressed in terms of the thermal conductivities $\kappa_{1,2}$ of the two materials and the segment lengths $L_{1,2}$ of the binary material system.

Since strain changes both κ and $d\kappa/dT$, it theoretically can cause thermal rectification in systems that are partially strained and partially unstrained. This chapter provides the theoretical background and evaluates thermal rectification in the hypothetical single material system that is partly strained and partly unstrained.

5.1.2. Theory

From classical heat transfer, the necessary condition for rectification is that $\kappa(T,\mathbf{r})$ be a non-separable function of temperature T and position $\mathbf{r}$. This is satisfied by a one-dimensional (1D) perfectly insulated bi-segment system with no interfacial thermal resistance and where $\kappa(T)$ for each material has a different temperature dependence [72]. Around room temperature, a linear relationship between κ and T is often a reasonable approximation for a broad range of materials and typically becomes more suitable as ΔT decreases. Thus, the thermal conductivity of each segment is $\kappa = aT + b$, where a and b are constants.

Let $\theta = (T - T_c)/(T_h - T_c)$ and $y = x/L$, where T_c and T_h denote the cold and hot boundary temperatures, and x and L are respectively the linear position and total length of the combined material system, as shown in Figure 22. Thus, θ and y vary between 0 and 1, and the dimensionless heat equation assumes the form,

$$\frac{d}{dy}(\hat{\kappa}_i \frac{d\theta}{dy}) = 0, \quad i = 1,\ 2, \qquad \text{(Eq.24)}$$

where, $\hat{\kappa}_i$ denotes the dimensionless thermal conductivity $\hat{\kappa}_i = \hat{a}_i\theta + \hat{b}_i$ with $\hat{a}_i = a_i(T_h - T_c)/\kappa_{ref}$ and $\hat{b}_i = \frac{(b_i + a_i T_c)}{\kappa_{ref}}$. The subscript i distinguishes the two material segments. For ease, we let $\kappa_{ref} = 1$ Wm^{-1}K^{-1}. $\hat{\kappa}_i$ is positive, i.e. $\hat{\kappa}_i > 0$, so $\hat{a}_i$ and $\hat{b}_i$ are constrained by (1) $\hat{a}_i > -\hat{b}_i$, and (2) $\hat{b}_i > 0$.

Since the system is in steady state and the heat flux in each segment is equal,

$$\hat{J}_F = -\frac{\int_0^{\theta_{int_F}} \hat{\kappa}_1(\theta) d\theta}{\int_0^f dy} = -\frac{\int_{\theta_{int_F}}^1 \hat{\kappa}_2(\theta) d\theta}{\int_f^1 dy} \qquad \text{(Eq.25)}$$

where $\hat{J}_F$ and θ_{int_F} respectively denote the dimensionless heat flux and interfacial temperature in the forward direction, and $0 \leq f \leq 1$ is the length fraction of M_1 compared with the combined length of the binary material system, as shown in Figure 22 (a). With $\hat{J}_R$ as the heat flux, the direction of the temperature gradient changes and the integration boundaries in the numerator are switched. Hence,

$$R = \frac{\hat{J}_{1F}}{\hat{J}_{1R}} = \frac{\hat{J}_{2F}}{\hat{J}_{2R}} = \frac{\hat{J}_{1F}}{\hat{J}_{2R}} = \frac{\hat{J}_{2F}}{\hat{J}_{1R}}, \text{ or}$$

$$R = \frac{\int_0^{\theta_{int_F}} \hat{\kappa}_1(\theta)d\theta}{\int_{\theta_{int_R}}^1 \hat{\kappa}_1(\theta)d\theta} = \frac{\int_{\theta_{int_F}}^1 \hat{\kappa}_2(\theta)d\theta}{\int_0^{\theta_{int_\mathrm{R}}} \hat{\kappa}_2(\theta)d\theta} = \frac{(1-f)\int_0^{\theta_{int_F}} \hat{\kappa}_1(\theta)d\theta}{f\int_0^{\theta_{int_\mathrm{R}}} \hat{\kappa}_2(\theta)d\theta} = \frac{f\int_{\theta_{int_F}}^1 \hat{\kappa}_2(\theta)d\theta}{(1-f)\int_{\theta_{int_R}}^1 \hat{\kappa}_1(\theta)d\theta}$$

(Eq. 26)

Eq.26 provides a solution for $R(\hat{a}_1,\ \hat{b}_1,\ \hat{a}_2,\ \hat{b}_2,\ f)$, hereinafter referred to as the *analytical solution* solved for in Appendix A. Eq. (26) is further simplified by noting that for any given material pair, maximum rectification occurs when $\theta_{\mathrm{int}_F} = \theta_{\mathrm{int}_R} = \theta_{\mathrm{int}}$[71] [73].

Figure 22 (b) presents the analytical solution for R for some example material combinations. The raw data used to determine $\hat{a}, \hat{b}$ is provided in Appendix B. The figure also reveals the sensitivity of R to f around its maximum value $R_{\max}$ (at f_{opt}). For example, (f_{opt}, $R_{\max}$) = (0.94, 1.61) for a Si-Ce binary system, which has the highest thermal rectification among the evaluated material combinations. The value of $|dR/df|$ is also large around $R_{\max}$, indicating high sensitivity to f which may make it experimentally challenging to achieve the highest thermal rectification due to the level of precision required while fabricating the device. The temperature profile for the Si-Ce system is presented in Figure 22 (c). By using f = 0.94 the system is optimized for R. Therefore, the intersection of the temperature profiles for $\hat{J}_F$ and $\hat{J}_R$occurs at the interface of the two materials (f_{opt}). Since the interface temperature is unchanged for both forward and reverse flux cases, $\hat{\kappa}_{1,2}(\theta_{\text{int}_F}) = \hat{\kappa}_{1,2}(\theta_{\text{int}_R}) = \hat{\kappa}_{1,2}(\theta_{\text{int}})$, as depicted in Figure 22 (d).

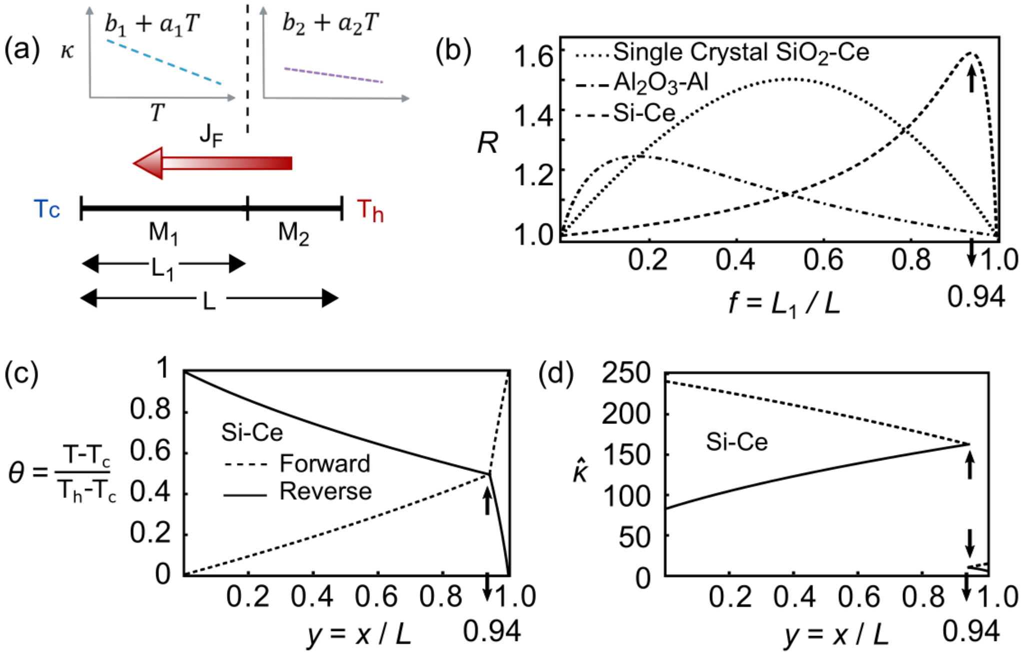

Figure 22. (a) Schematic diagram of a 1D binary material system under *forward-biased* boundary conditions. During the reverse-biased simulations T_c and T_h are switched. The requirement for thermal rectification is that $\frac{d\kappa_1}{dT} \neq \frac{d\kappa_2}{dT}$. (b) Analytical solution of $R(f)$. Three sample material combinations are selected to illustrate different curvatures about f_{opt} and hence the sensitivity of R around $R_{\max}$, which is the maximum value of R attainable for each material combination. The arrows indicate the location of f_{opt} for Si-Ce and the corresponding location of $R_{\max}$. (c) Dimensionless temperature and (d)

thermal conductivity profiles of the Si-Ce material system designed using f_{opt}. Figure modified from [29].

A material may have a strain gradient caused either extrinsically or intrinsically. The latter is often seen in thin films and nanostructures due to the mismatch in lattice constant or mismatch in thermal expansion coefficients during their deposition and growth.

5.1.3. Results and discussion

Heterostructure free-standing nanowires can exhibit strain at the interface, which, due to their high aspect ratio, is relieved laterally a short distance away from that interface. Thus, a strain-relaxed transition can also be produced within a single material. [74],[75]

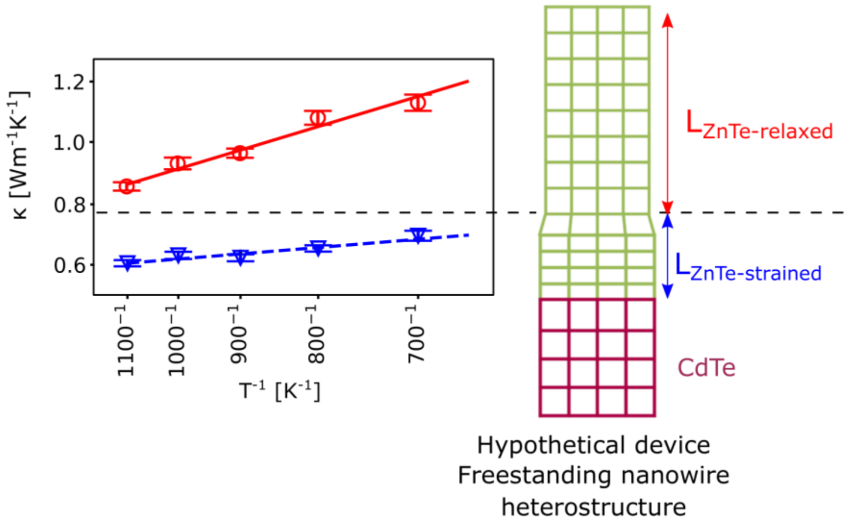

Figure 23. A hypothetical free-standing axial nanowire heterostructure, creating a strained-relaxed ZnTe junction in the vicinity of the ZnTe-CdTe interface. The data is from simulations of the strained and relaxed ZnTe films in Chapter 2. The different $d\kappa/dT$ slopes suggest that thermal rectification is possible within the ZnTe portion of the

hypothetical nanowire. L refers to the length fractions of each of these strained and relaxed portions. The grid provides a visualization of the unit cell spacing in the various structures and the type of strain present.

Consider the hypothetical case of a compositionally uniform one-dimensional material that is partly strained and partly unstrained. This resembles the ZnTe portion of Figure 23. Linear fits to the $\kappa(T)$ data in Figure 23 lead to the relations, $\kappa_{\mathrm{ZnTe,s}} = 1.169 - 0.0005T$ and $\kappa_{\mathrm{ZnTe,r}} = 2.21 - 0.001T$ W m^{-1} K^{-1}. The subscript s and r denote strained and relaxed films respectively. Next, both R and the optimized length fraction are calculated using the analytical relations in Appendix A [29]. For $T_c = 680$ K and $T_h = 720$ K, the strained-unstrained ZnTe bisegment structure rectifies heat flux along the axial direction by 0.1% with a length fraction of $\frac{L_{\mathrm{ZnTe,s}}}{L_{\mathrm{ZnTe,r}}} = 0.35$. This is a relatively small value for rectification since $T \gg \theta_{\mathrm{D}}$ and so $\frac{d\kappa}{dT} \approx 0$ across both the strained and unstrained segment. At temperatures below θ_{D}, R should increase since $\kappa(T)$ is now an exponential function of T. [76] Note that R is material dependent, although it typically increases with increasing ΔT. [76] At the nanoscale, an asymmetric geometry also induces rectification. [77],[78].

5.2. Future work

Utilizing nanowires for thermal rectification is not limited to the aforementioned axial heterostructures. Nanowires offer wide-ranging possibilities for novel heterostructure design and strain engineering. Recently, highly asymmetric GaAs/$Al_{0.5}In_{0.5}As$ core-shell nanowires have been synthesized so that the nanowires are bent over in a controllable manner due to the stress/strain caused by their configuration as shown in Figure 24. [79] This approach creates a spatially varying strain fields over a larger volume, providing new opportunities to design more efficient thermal rectifiers. Other than altering thermal conduction, strain also changes and enhances the mobility of charge carriers[80], [81], [82], [83] which may be of particular use for thermoelectric devices since their performance figure of merit is given by $ZT = \sigma S T/\kappa$, i.e. it is proportional to electrical conductivity σ, the Seebeck coefficient S, and is inversely proportional to κ. By selecting the appropriate materials, material combinations, and their thicknesses, it is possible to tune the type and extent of strain and therefore their electrical and thermal response and increase the figure of merit. The problem is complicated by the challenges in both simulating and experimentally measuring these properties but can be very useful in excelling the field of thermoelectric devices and opens new doors in the realm of thermal rectifiers.

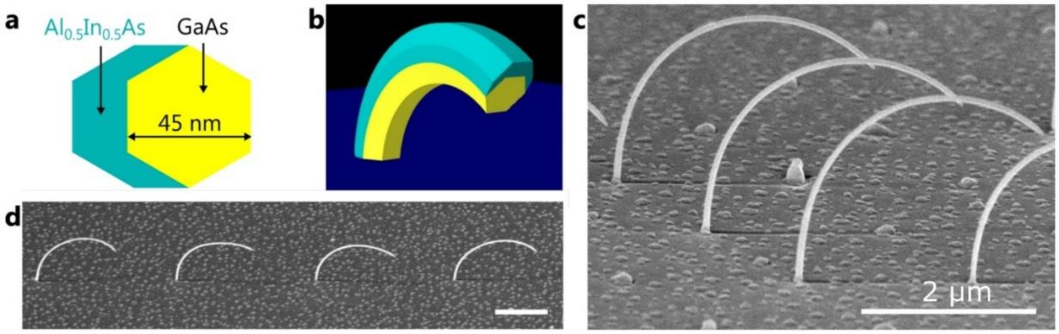

Figure 24. (a) and (b) Schematic illustration of the bent nanowire heterostructure consisting of a 45 nm GaAs core and a 20 nm $Al_{0.5}In_{0.5}As$ shell. (c) and (d) Scanning electron microscopy images of the bent nanowires. Reprinted (adapted) with permission from [79]. Copyright 2018 American Chemical Society.

Appendix A - Analytical Solution for *R*

Determine $\theta_{\mathrm{int_R}}$ by substituting $\hat{a}_1, \hat{b}_1, \hat{a}_2, \hat{b}_2$, and f into (A.1). For readability, the hat has been dropped in equations (A.1) and (A.2). The realizable solution for $\theta_{\mathrm{int_R}}$ lies between 0 and 1. This solution is used in (A.2) to find $\theta_{\mathrm{int}_F} \in [0,1]$. Subsequently, R is computed from the right hand side of equation (A.3), i.e.,[29]

$$\theta_{\mathrm{int_R}} = \frac{b_1 - f b_1 + f b_2 \pm 0.5\sqrt{-4(-1+f)(a_1 - a_1 f + a_2 f)(a_1 + 2b_1) + 4(b_1 - f b_1 + f b_2)^2}}{a_1(-1+f) - a_2 f}, \tag{A.1}$$

$$\begin{aligned}
\theta_{\mathrm{int}_F} = {} & \frac{1}{2a_2(-1+\theta_{\mathrm{int}_R})b_1 - a_1(a_2 + 2\theta_{\mathrm{int}_R} b_2)} \\
& \times [a_2 \theta_{\mathrm{int}_R}{}^2 b_1 + (a_1 - a_1\theta_{\mathrm{int}_R}{}^2 + 2b_1)b_2 \\
& \pm \sqrt{[b_1^2(a_2^2(4 + \theta_{\mathrm{int}_R}(-8 + 4\theta_{\mathrm{int}_R} + \theta_{\mathrm{int}_R}{}^3))} \\
& + 4a_2(2 + \theta_{\mathrm{int}_R}(-4 + 3\theta_{\mathrm{int}_R}))b_2 + 4b_2^2) \\
& - 2a_1(-1 + \theta_{\mathrm{int}_R})b_1(-a_2^2(-2 + \theta_{\mathrm{int}_R}{}^2) \\
& + a_2(1 + \theta_{\mathrm{int}_R})(4 + (-2 + \theta_{\mathrm{int}_R})\theta_{\mathrm{int}_R})b_2 \\
& + 2(1 + 3\theta_{\mathrm{int}_R})b_2^2) - a_1^2(-1 + \theta_{\mathrm{int}_R}{}^2) \\
& \times (a_2^2 + 2a_2(1 + \theta_{\mathrm{int}_R})b_2 + (1 - (-4 + \theta_{\mathrm{int}_R})\theta_{\mathrm{int}_R})b_2^2)]]
\end{aligned} \quad \text{, and} \tag{A.2}$$

$$R = \frac{\int_0^{\theta_{int_F}} \hat{\kappa}_1(\theta)d\theta}{\int_{\theta_{int_R}}^1 \hat{\kappa}_1(\theta)d\theta} = \frac{(\hat{a}_1\theta_{int_F} + 2\hat{b}_1)\theta_{int_F}}{(\hat{a}_1 + \hat{a}_1\theta_{int_R} + 2\hat{b}_1)(1 - \theta_{int_R})} \quad . \tag{A.3}$$

These and subsequent simplifications were also verified using Mathematica [84].

Appendix B: Raw temperature - thermal conductivity data

Table B1. Data used to calculate the linear best fit for the temperature dependence of thermal conductivity for various materials. Unless otherwise specified, the data corresponds to the recommended values presented in reference [85].

Material	T[K]	κ [$Wm^{-1}K^{-1}$]	Error	Notes
Ce	200	5	+/-5-15%	Polycrystalline, 99.6% purity
	250	5.83	+/-5-15%	
	263	6.02	+/-5-15%	
	263	10.5	+/-5-15%	
	273.2	10.8	+/-5%	
	300	11.4	+/-5%	
	350	12.4	+/-5-15%	
	400	13.3	+/-5-15%	
Al	200	237	+/- 3-5%	99.9999% purity, well-annealed
	250	235	+/- 3-5%	
	273.2	236	+/- 3-5%	
	300	237	+/- 2-3%	
	350	240	+/- 3-5%	
	400	240	+/- 3-5%	
Single Crystal SiO_2	200	16.4	+-5-10%	Parallel to c-axis
	250	12.7	+-5-10%	
	273	11.6	+-5-10%	
	300	10.4	+-5%	
	350	8.8	+-5%	
	400	7.6	+-5%	
Si	200	264	+/-4-10%	High purity
	250	191	+/-4-10%	
	273.2	168	+/-4%	
	300	148	+/-4-10%	
	350	119	+/-4-10%	
	400	98.9	+/-4-10%	
Al_2O_3	200	82	+/-10-15%	High purity synthetic sapphire, single crystal
	250	58	+/-10-15%	
	273.2	52	+/-10-15%	
	300	46	+/-10-15%	
	350	38	+/-10-15%	
	400	32.4	+/-10-15%	

Chapter 6. Summary

Chapter 2 studies the significance of heteroepitaxial strain on altering thermal conduction. It does so by MD simulations of the physical vapor deposition of ZnTe on $Cd_{1-\alpha}Zn_{\alpha}Te$, where α = 0 or 1 and the interatomic potential for both compounds is defined by an SW function [43]. Non-equilibrium MD simulations are used to determine the thermal conductivity of the relaxed and strained deposited ZnTe crystal. Given the promise of these results, Chapter 3 further simulates different thin film thicknesses and different amounts of strain, both biaxial and uniform, to develop a general understanding of the effect of strain on thermal conduction. In Chapter 4, parameters for validating the potential function for thermomechanical MD simulations is discussed and its importance is highlighted. Chapter 5 uses strain to induce thermal rectification in a new way and Chapter 6 provides a summary of the thesis.

Given the limitations of the SW potential function and the case-study of ZnTe, it is important to capture the most extendable conclusions of this thesis for future simulations and experimental research in other material systems. In the context of crystalline semiconducting or insulating solids, the most general conclusions are listed below. Some overlap with existing literature that are based on different materials or methods, while some are not reported in any context to the knowledge of the author. Those are marked by "*" symbol.

1. Strain strongly impacts thermal conduction. Its impact depends on the type of strain, compression or dilation, biaxial or uniform, and on the material.

2. When the finite size of a film with perfectly diffuse boundaries, becomes comparable to the mean free path of the thermal vibrations, finite size vastly reduces thermal conduction.

3*. The trends for $\kappa(\epsilon)$ depend on the finite thickness of the film and the type of strain, i.e. compression or dilations, and biaxial or uniform:

3.1*. As the thickness of the film decreases, the magnitude of κ decreases until boundary scattering completely dominants. In this case, $\kappa(\epsilon)$ will depend on $v_g(\epsilon)$. This is shown in Chapters 2 and 3 to justify the trends of κ and κ_x for 19 unit cell films under uniform or biaxial tension and for κ_z under both biaxial compression and tension.

3.2*. For a given material, the thickness at which boundary scattering dominates depends on the type of strain, i.e. compression or tension, and biaxial or uniform. For example, in Chapter 3, the 19 unit cell film exhibits a decline in κ under uniform compression, attributed to increased Umklapp scattering which reduces the mean free path of the vibrations and lowers the thickness at which boundary scattering dominates.

This conclusion is of importance as it suggests that if a film is thin enough so that boundary scattering dominates, then one can predict the behavior of $\kappa(\epsilon)$ based on the bulk dispersion curve alone, which could greatly simplify device design.

4*. A single material that is partially strained and partially unstrained, can theoretically act as a thermal rectifier. The strain may be due to strain-relaxation along a nanowire or it could be caused simply by flexing a material.

The following future work is thought to be of value to the scientific community:

1. Understanding the limits of conclusion (3) in the context of other materials and testing its validity for thinner films.

2. Developing interatomic potentials intended for thermomechanical behavior of crystals that account for fundamental properties such as thermal wave dispersion and the Grüneisen parameter in a computationally efficient manner so that size-dependent studies, such as those in this thesis, are feasible.

3. Engineering strain in a core-shell heterostructure, for application to thermal rectifiers or thermoelectric devices. This is a scientifically rich and promising field of study which requires theoretical development, simulations, and experimental research to evolve.

References

[1] T. Majdi, S. Pal, A. Hafreager, S. Murad, R. P. Sahu, and I. K. Puri, “Altering thermal transport by strained-layer epitaxy,” *Appl. Phys. Lett.*, vol. 112, no. 19, 2018.

[2] J. M. Ziman, *Electrons and Phonons: the theory of transport phenomena in solids*. Great Britain: Clarendon Press, 1960.

[3] D. P. Sellan, E. S. Landry, J. E. Turney, A. J. H. McGaughey, and C. H. Amon, “Size effects in molecular dynamics thermal conductivity predictions,” *Phys. Rev. B*, vol. 81, no. 21, p. 214305, Jun. 2010.

[4] C. Kittel, *Introduction to Solid State Physics*, Eighth. United States of America: John Wiley & Sons, 2005.

[5] N. W. Ashcroft and N. D. Mermin, “Solid State Physics,” *Solid State Physics*. 1976.

[6] C. B. Walker, “X-Ray Study of Lattice Vibrations in Aluminum,” *Phys. Rev.*, vol. 103, no. 3, pp. 547–557, Aug. 1956.

[7] R. W. Keyes, “Trends in the Lattice ‘Combination Bands’’ of Zincblende-type Semiconductors,’” *J. Chem. Phys.*, vol. 37, no. 1, pp. 72–73, Jul. 1962.

[8] D. Hurley, S. L. Shinde, and E. S. Piekos, “Interaction of thermal phonons with interfaces,” in *Length-Scale Dependent Phonon Interactions*, S. L. Shinde and G. P. Srivastava, Eds. Springer, 2014.

[9] A. McGaughey, “Predicting phonon properties from equilibrium molecular dynamics simulations,” *Annu. Rev. Heat Transf.*, pp. 1–65, 2012.

[10] P. W. Bridgman, “The thermal conductivity and compressibility of several rocks under high pressures,” *Am. J. Sci.*, vol. 7, no. 38, pp. 81–102, 1924.

[11] D. S. Hughes and F. Sawin, “Thermal Conductivity of Dielectric Solids at High Pressure,” *Phys. Rev.*, vol. 161, no. 3, pp. 861–863, Sep. 1967.

[12] B. Håkansson, P. Andersson, and G. Bäckström, “Improved hot-wire procedure for thermophysical measurements under pressure,” *Rev. Sci. Instrum.*, vol. 59, no. 10, pp. 2269–2275, Oct. 1988.

[13] S. Andersson and G. Backstrom, “The thermal conductivity and heat capacity of single-crystal Si under hydrostatic pressure,” *J. Phys. C Solid State Phys.*, vol. 21, no. 20, pp. 3727–3735, Jul. 1988.

[14] D. A. Dalton, W.-P. Hsieh, G. T. Hohensee, D. G. Cahill, and A. F. Goncharov, “Effect of mass disorder on the lattice thermal conductivity of MgO periclase under pressure,” *Sci. Rep.*, vol. 3, no. 1, p. 2400, Dec. 2013.

[15] S. Bhowmick and V. B. Shenoy, “Effect of strain on the thermal conductivity of solids,” *J. Chem. Phys.*, vol. 125, p. 164513, 2006.

[16] X. Li, K. Maute, M. L. Dunn, and Y. Ronggui, “Strain effects on the thermal conductivity of nanostructures,” *Phys. Rev. B*, vol. 81, no. 24, p. 245318, 2010.

[17] R. C. Picu, T. Borca-Tasciuc, and M. C. Pavel, “Strain and size effects on heat transport in nanostructures,” *J. Appl. Phys.*, vol. 93, no. 6, pp. 3535–3539, Mar. 2003.

[18] L. Lindsay, D. A. Broido, J. Carrete, N. Mingo, and T. L. Reinecke, "Anomalous pressure dependence of thermal conductivities of large mass ratio compounds," *Phys. Rev. B*, vol. 91, no. 12, p. 121202, Mar. 2015.

[19] G. A. Slack, "The Thermal Conductivity of Nonmetallic Crystals," *Solid State Phys. - Adv. Res. Appl.*, vol. 34, no. C, pp. 1–71, 1979.

[20] G. A. Slack and P. Andersson, "Pressure and temperature effects on the thermal conductivity of CuCl," *Phys. Rev. B*, vol. 26, no. 4, pp. 1873–1884, Aug. 1982.

[21] G. A. Slack, "Thermal conductivity of ice," *Phys. Rev. B*, vol. 22, no. 6, pp. 3065–3071, Sep. 1980.

[22] T. Basak, M. N. Rao, M. K. Gupta, and S. L. Chaplot, "Vibrational properties and phase transitions in II–VI materials: lattice dynamics, ab initio studies and inelastic neutron scattering measurements," *J. Phys. Condens. Matter*, vol. 24, no. 11, p. 115401, Mar. 2012.

[23] N. V. Lugueva, N. L. Kramynina, and S. M. Luguev, "Heat conductivity of polycrystalline ZnS under uniform compression," *Phys. Solid State*, vol. 43, no. 2, pp. 231–234, Feb. 2001.

[24] T. Ouyang and M. Hu, "Competing mechanism driving diverse pressure dependence of thermal conductivity of X Te (X = Hg , Cd , and Zn)," *Phys. Rev. B*, vol. 92, no. 23, p. 235204, Dec. 2015.

[25] X. C. Tong, *Advanced Materials for Thermal Management of Electronic Packaging*, Vol. 30. Springer Science & Business Media, 2011.

[26] D. M. Rowe, *Thermoelectrics Handbook: Macro to Nano*. CRC, Taylor & Francis, 2005.

[27] M. Liangruksa and I. K. Puri, “Phonon transport in an initially twisted polyvinyl acetate nanofiber,” *Appl. Phys. Lett.*, vol. 102, no. 19, p. 191907, 2013.

[28] H. Y. Lv, W. J. Lu, D. F. Shao, H. Y. Lu, and Y. P. Sun, “Strain-induced enhancement in the thermoelectric performance of a ZrS 2 monolayer,” *J. Mater. Chem. C*, vol. 4, no. 20, pp. 4538–4545, 2016.

[29] T. Majdi, S. Pal, and I. K. Puri, “Recipe for optimizing a solid-state thermal rectifier,” *Int. J. Therm. Sci.*, vol. 117, pp. 260–265, 2017.

[30] S. Murad and I. K. Puri, “A thermal logic device based on fluid-solid interfaces,” *Appl. Phys. Lett.*, vol. 102, no. 19, p. 193109, 2013.

[31] J. Ravichandran *et al.*, “Crossover from incoherent to coherent phonon scattering in epitaxial oxide superlattices,” *Nat. Mater.*, vol. 13, no. 2, pp. 168–172, 2014.

[32] J. Ravichandran *et al.*, “Crossover from incoherent to coherent phonon scattering in epitaxial oxide superlattices,” *Nat. Mater. - Suppl. Inf.*, vol. 13, no. 2, pp. 168–172, 2014.

[33] A. R. Abramson, C.-L. Tien, and A. Majumdar, “Interface and strain effects on the thermal conductivity of heterostructures: a molecular dynamics study,” *J. Heat Transfer*, vol. 124, no. 5, p. 963, 2002.

[34] Y. Gao, Q. Liu, and B. Xu, “Lattice Mismatch Dominant Yet Mechanically Tunable

Thermal Conductivity in Bilayer Heterostructures," *ACS Nano*, vol. 10, no. 5, pp. 5431–5439, 2016.

[35] X. W. Zhou, J. J. Chavez, S. Almeida, and D. Zubia, "Understanding misfit strain releasing mechanisms via molecular dynamics simulations of CdTe growth on {112} zinc-blende CdS," *J. Appl. Phys.*, vol. 120, no. 4, p. 045304, 2016.

[36] A. S. Henry and G. Chen, "Spectral Phonon Transport Properties of Silicon Based on Molecular Dynamics Simulations and Lattic Dynamics," *J. Comput. Theor. Nanosci.*, vol. 5, no. 2, pp. 141–152, 2008.

[37] M. Ohring, *Materials Science of Thin Films - Deposition and Structures*, 2nd ed. Academic Press, 2002.

[38] B. Späth, J. Fritsche, F. Säuberlich, A. Klein, and W. Jaegermann, "Studies of sputtered ZnTe films as interlayer for the CdTe thin film solar cell," *Thin Solid Films*, vol. 480–481, pp. 204–207, 2005.

[39] M. R. H. Khan, "Interface properties of a CdTe-ZnTe heterojunction," *J. Phys. D. Appl. Phys.*, vol. 27, no. 10, p. 2190, 1994.

[40] J. R. Rumble, Ed., *CRC Handbook of Chemistry and Physics*, 98th ed. CRC Press, 2017.

[41] G. A. Slack, "Thermal conductivity of II-VI compounds and phonon scattering by Fe2+ Impurities," *Phys. Rev. B*, vol. 6, no. 10, pp. 3791–3800, 1971.

[42] S. Plimpton, "Plimpton_FastParallelAlgorithmsForShortRangeMD_1995.pdf," *J.*

Comput. Phys., vol. 117, no. 1, pp. 1–19, 1995.

[43] X. W. Zhou, D. K. Ward, J. E. Martin, F. B. Van Swol, J. L. Cruz-Campa, and D. Zubia, “Stillinger-Weber potential for the II-VI elements Zn-Cd-Hg-S-Se-Te,” *Phys. Rev. B - Condens. Matter Mater. Phys.*, vol. 88, no. 8, p. 085309, 2013.

[44] X. W. Zhou *et al.*, “An atomistically validated continuum model for strain relaxation and misfit dislocation formation,” *J. Mech. Phys. Solids*, vol. 91, pp. 265–277, 2016.

[45] W. Shinoda, M. Shiga, and M. Mikami, “Rapid estimation of elastic constants by molecular dynamics simulation under constant stress,” *Phys. Rev. B*, vol. 69, no. 13, p. 134103, Apr. 2004.

[46] M. E. Tuckerman, J. Alejandre, R. López-Rendón, A. L. Jochim, and G. J. Martyna, “A Liouville-operator derived measure-preserving integrator for molecular dynamics simulations in the isothermal–isobaric ensemble,” *J. Phys. A. Math. Gen.*, vol. 39, no. 19, pp. 5629–5651, May 2006.

[47] X. W. Zhou *et al.*, “High-fidelity simulations of CdTe vapor deposition from a bond-order potential-based molecular dynamics method,” *Phys. Rev. B - Condens. Matter Mater. Phys.*, vol. 85, no. 24, p. 245302, 2012.

[48] H. P. Singh and B. Dayal, “Lattice parameters and thermal expansion of zinc telluride and mercury selenide,” *Acta Crystallogr. Sect. A Cryst. Phys. Diffr.*, vol. 26, no. 3, pp. 363–364, 1970.

[49] M. G. Williams, R. D. Tomlinson, and M. J. Hampshire, “X-ray determination of the lattice parameters and thermal expansion of cadmium telluride in the

temperature range 20-420 C," *Solid State Commun.*, vol. 7, no. 24, pp. 1831–1832, 1969.

[50] M. Thomas, *Theoretical Modeling of Vibrational Spectra in the Liquid Phase*. Springer, 2017.

[51] *Power Spectra Estimation*. National Semiconductor Application Note 255, 1980.

[52] F. W. Isen, *DSP for MATLAB^{TM} and LabVIEW^{TM} Volume I: Fundamentals of Discrette Signal Processing*, vol. I. Morgan & Claypool Publishers, 2008.

[53] *numpy.fft.fft*. The SciPy Community, 2018.

[54] *numpy.conj*. The SciPy Community, 2018.

[55] D. M. Mattox, "Particle bombardment effects on thin-film deposition: A review," *J. Vac. Sci. Technol. A Vacuum, Surfaces, Film.*, vol. 7, no. 3, pp. 1105–1114, 1989.

[56] D. Rioux, D. W. Niles, and H. Höchst, "ZnTe: A potential interlayer to form low resistance back contacts in CdS/CdTe solar cells," *J. Appl. Phys.*, vol. 73, no. 12, pp. 8381–8385, 1993.

[57] S. Tatarenko, P. H. Jouneau, K. Saminadayar, and J. Eymery, "Investigation of the epitaxial growth mechanism of ZnTe on (001) CdTe," *J. Appl. Phys.*, vol. 77, no. 7, pp. 3104–3110, 1995.

[58] K. Kusaba, L. Galoisy, Y. Wang, M. T. Vaughan, and D. J. Weidner, "Determination of phase transition pressures of ZnTe under quasihydrostatic conditions," *Pure Appl. Geophys. PAGEOPH*, vol. 141, no. 2–4, pp. 643–652, 1993.

[59] H. Bao, X. L. Ruan, and M. Kaviany, “Theory of the broadening of vibrational spectra induced by lowered symmetry in yttria nanostructures,” *Phys. Rev. B - Condens. Matter Mater. Phys.*, vol. 78, no. 12, p. 125417, 2008.

[60] M. Hu, X. Zhang, and D. Poulikakos, “Anomalous thermal response of silicene to uniaxial stretching,” *Phys. Rev. B - Condens. Matter Mater. Phys.*, vol. 87, no. 19, p. 195417, 2013.

[61] H. J. Maris and S. Tamura, “Heat flow in nanostructures in the Casimir regime,” *Phys. Rev. B*, vol. 85, no. 5, p. 054304, Feb. 2012.

[62] Hynes and Willimiam, *CRC Handbook of Chemistry and Physics*, 92nd ed. Boca Raton, FL: CRC Press, 2011.

[63] P. K. Schelling, S. R. Phillpot, and P. Keblinski, “Comparison of atomic-level simulation methods for computing thermal conductivity,” *Phys. Rev. B - Condens. Matter Mater. Phys.*, vol. 65, no. 14, pp. 1–12, 2002.

[64] L. T. Kong, “Phonon dispersion measured directly from molecular dynamics simulations,” *Comput. Phys. Commun.*, vol. 182, no. 10, pp. 2201–2207, 2011.

[65] “scipy.signal.savgol_filter,” 2015. [Online]. Available: https://docs.scipy.org/doc/scipy-0.15.1/reference/generated/scipy.signal.savgol_filter.html. [Accessed: 14-Aug-2019].

[66] F. H. Stillinger and T. A. Weber, “Computer simulation of local order in condensed phases of silicon,” *Phys. Rev. B*, vol. 31, no. 8, p. 5262, 1985.

[67] N. Vagelatos, D. Wehe, and J. S. King, "Phonon dispersion and phonon densities of states for ZnS and ZnTe," *J. Chem. Phys.*, vol. 60, no. 9, p. 3613, 1974.

[68] J. Camacho, I. Loa, A. Cantarero, and K. Syassen, "Vibrational properties of ZnTe at high pressures," *J. Phys. Condens. Matter*, vol. 14, no. 4, pp. 739–757, Feb. 2002.

[69] L. J. Porter, J. F. Justo, and S. Yip, "The importance of Grüneisen parameters in developing interatomic potentials," *J. Appl. Phys.*, vol. 82, no. 11, pp. 5378–5381, Dec. 1997.

[70] N. A. Roberts and D. G. Walker, "A review of thermal rectification observations and models in solid materials," *Int. J. Therm. Sci.*, vol. 50, no. 5, pp. 648–662, 2011.

[71] T.-M. Shih, Z. Gao, Z. Guo, H. Merlitz, P. J. Pagni, and Z. Chen, "Maximal rectification ratios for idealized bi-segment thermal rectifiers," *Sci. Rep.*, vol. 5, 2015.

[72] D. B. Go and M. Sen, "On the condition for thermal rectification using bulk materials," *J. Heat Transfer*, vol. 132, no. 12, p. 124502, 2010.

[73] T. Takeuchi, "Very large thermal rectification in bulk composites consisting partly of icosahedral quasicrystals," *Sci. Technol. Adv. Mater.*, vol. 15, no. 6, p. 064801, 2014.

[74] M. W. Larsson *et al.*, "Strain mapping in free-standing heterostructured wurtzite InAs/InP nanowires," *Nanotechnology*, vol. 18, no. 1, p. 015504, 2007.

[75] M. De La Mata, C. Magén, P. Caroff, and J. Arbiol, "Atomic scale strain relaxation

in axial semiconductor III-V nanowire heterostructures," *Nano Lett.*, vol. 14, no. 11, pp. 6614–6620, 2014.

[76] C. Dames, "Solid-state thermal rectification with existing bulk materials," *J. Heat Transfer*, vol. 131, no. 6, p. 61301, 2009.

[77] Y. Wang, A. Vallabhaneni, J. Hu, B. Qiu, Y. P. Chen, and X. Ruan, "Phonon lateral confinement enables thermal rectification in asymmetric single-material nanostructures," *Nano Lett.*, vol. 14, no. 2, pp. 592–596, 2014.

[78] S. Pal and I. K. Puri, "Thermal AND Gate Using a Monolayer Graphene Nanoribbon," *Small*, vol. 11, no. 24, pp. 2910–2917, 2015.

[79] R. B. Lewis, P. Corfdir, H. Küpers, T. Flissikowski, O. Brandt, and L. Geelhaar, "Nanowires Bending over Backward from Strain Partitioning in Asymmetric Core–Shell Heterostructures," *Nano Lett.*, vol. 18, no. 4, pp. 2343–2350, Apr. 2018.

[80] E. Ungersboeck, S. Dhar, G. Karlowatz, V. Sverdlov, H. Kosina, and S. Selberherr, "The Effect of General Strain on the Band Structure and Electron Mobility of Silicon," *Electron Devices, IEEE Trans.*, vol. 54, no. 9, pp. 2183–2190, 2007.

[81] P. R. Chidambaram, C. Bowen, S. Chakravarthi, C. Machala, and R. Wise, "Fundamentals of Silicon Material Properties for Successful Exploitation of Strain Engineering in Modern CMOS Manufacturing," *IEEE Trans. Electron Devices*, vol. 53, no. 5, pp. 944–964, 2006.

[82] A. Nainani, D. Kim, T. Krishnamohan, and K. Saraswat, "Hole mobility and its enhancement with strain for technologically relevant III-V semiconductors," in

International Conference on Simulation of Semiconductor Processes and Devices, IEEE, 2009, pp. 47–50.

[83] R. Sharma and A. K. Rana, “Strained Si: opportunities and challenges in nanoscale MOSFET,” in *2015 IEEE 2nd International Conference on Recent Trends in Information Systems (ReTIS)*, 2015, pp. 475–480.

[84] I. Wolfram Research, “Mathematica,” vol. Version 10. Wolfram Research, Inc. , Champaign, Illionis, 2015.

[85] Y. S. Touloukian and P. University, *Thermophysidal Properties Of Matter: The TPRC Data Series; a Comprehensive Compilation of Data*, vol. 1 and 2. New York: IFI/Plenum, 1970.